Accepted Manuscript

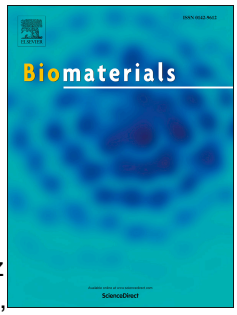

Effective cancer immunotherapy in mice by polyIC-imiquimod complexes and engineered magnetic nanoparticles

Ana Isabel Bocanegra Gondan, Ane Ruiz-de-Angulo, Aintzane Zabaleta, Nina Gómez Blanco, Beatriz Macarena Cobaleda-Siles, María Jesús Garcia-Granda, Daniel Padro, Jordi Llop, Blanca Arnaiz, María Gato, David Escors, Juan C. Mareque-Rivas

PII: S0142-9612(18)30241-2

DOI: 10.1016/j.biomaterials.2018.04.003

Reference: JBMT 18589

To appear in: *Biomaterials*

Received Date: 25 January 2018

Revised Date: 21 March 2018

Accepted Date: 1 April 2018

Please cite this article as: Bocanegra Gondan AI, Ruiz-de-Angulo A, Zabaleta A, Gómez Blanco N, Cobaleda-Siles BM, Garcia-Granda MaríJesú, Padro D, Llop J, Arnaiz B, Gato Marí, Escors D, Mareque-Rivas JC, Effective cancer immunotherapy in mice by polyIC-imiquimod complexes and engineered magnetic nanoparticles, *Biomaterials* (2018), doi: 10.1016/j.biomaterials.2018.04.003.

magnetic nanoparticles

*Ana Isabel Bocanegra Gondan,[1] Ane Ruiz-de-Angulo,[1] Aintzane Zabaleta,[1] Nina Gómez Blanco,[1] Beatriz Macarena Cobaleda-Siles,[1] María Jesús Garcia-Granda,[1] Daniel Padro,[1] Jordi Llop,[2] Blanca Arnaiz,[2] María Gato,[4] David Escors[4] and Juan C. Mareque-Rivas[1,2,3]**

[1]CIC biomaGUNE

Paseo Miramón 182, 20014 San Sebastián, Spain

[2]IKERBASQUE, Basque Foundation for Science

48011 Bilbao, Spain

[3]Department of Chemistry and Centre for NanoHealth

Swansea University, Singleton Park, Swansea, SA2 8PP, U.K.

[4] Department of Oncology, Navarrabiomed-Biomedical Research Centre,
Fundación Miguel Servet, Complejo Hospitalario de Navarra, Pamplona, Spain

**Email: juan.mareque-rivas@swansea.ac.uk*

Keywords: magnetic nanoparticles, drug delivery, Toll-like receptor agonists, vaccines, multimodal imaging, immunotherapy, checkpoint inhibition

ABSTRACT: Encouraging results are emerging from systems that exploit Toll like receptor (TLR) signaling, nanotechnology, checkpoint inhibition and molecular imaging for cancer immunotherapy. A major remaining challenge is developing effective, durable and tumour-specific immune responses without systemic toxicity. Here, we report a simple and versatile system based on synergistic activation of immune responses and direct cancer cell killing by combined TLR ligation using polyIC as TLR3 and imiquimod (R837) as TLR7 agonist, in combination with the model antigen ovalbumin (OVA) and phospholipid micelles loaded with zinc-doped iron oxide magnetic nanoparticles (MNPs). The combination of TLR agonists triggered a strong innate immune response in the lymph nodes (LNs) without systemic release of

melanoma cells expressing OVA, which was improved with immune checkpoint abrogation of the immunosuppressive programmed death-ligand 1 (PD-L1) at the level of the cancer cells. By magnetic resonance (MR) and nuclear imaging we could track the vaccine migration from the site of injection to LNs and tumour. Overall, we show this synergistic TLR agonists and their combination with MNPs and immune checkpoint blockade to have considerable potential for preclinical and clinical development of vaccines for cancer immunotherapy.

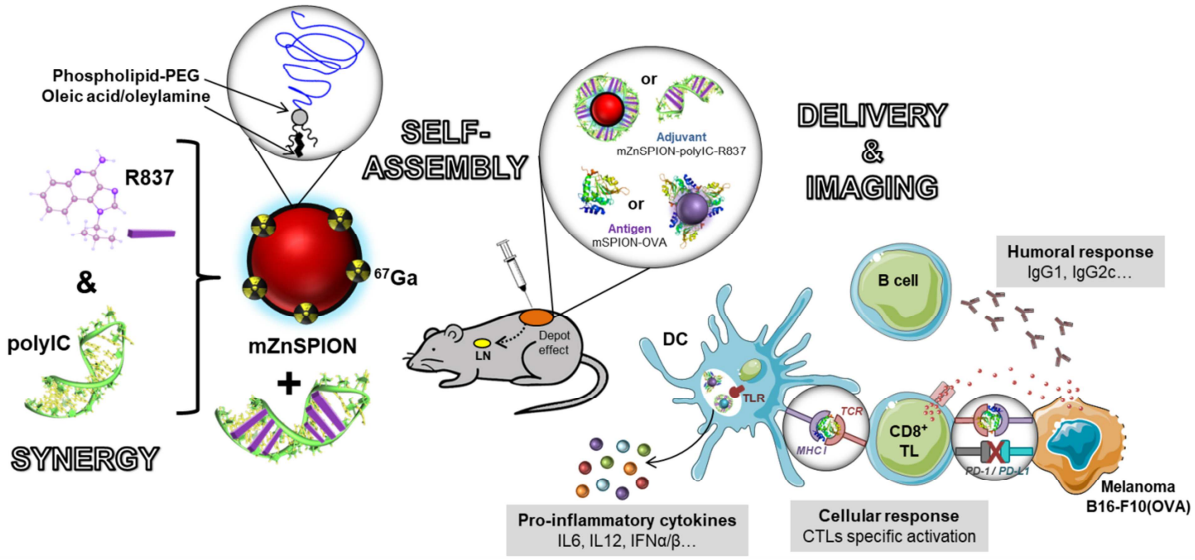

Introduction

Nanoparticles (NPs) used as delivery vehicles of single chemotherapy drugs have led so far to nanomedicines that mainly decrease treatment-induced side effects in patients.[1–3] Although NPs have also been used as a promising platform for improving combination drug therapy, enabling multidrug treatments that are limited by lack of efficacy and toxicity concerns,[4] improving the overall survival of patients with these systems remains a major challenge. These cancer nanomedicines are still severely limited by the barriers and characteristics of the

encounters with the immune system.[5,6]

As nanomedicine matures and the understanding of the immune system deepens, a growing number of studies are beginning to focus on engineering nanomaterials that can be applied for modulating and controlling/enhancing immune responses to improve therapies and treatments for cancer, infectious disease, and autoimmunity.[7–16],[17] Advancing the development of such immunomodulatory drug-loaded NPs targeting immune cells offers the advantage that drug payload delivery to even a small fraction of immune cells may be enough to achieve robust antitumour efficacy.[18] This is because immune cells can extensively proliferate and acquire the capacity to generate effective antitumour responses with memory against cancer cells through coordinated activation of innate and adaptive immune responses upon contact with the immunomodulatory NP. This offers unique and intriguing possibilities for tackling metastatic disease and developing durable, long-term defense against cancer – the holy grail of cancer research. Intrinsic imaging features of drug vehicles are ideal for evaluation of drug delivery efficiency and guiding and non-invasive monitoring of treatment responses. Although immune modulating gold NPs have been developed to enable computed tomography (CT) tracking, the amount of NP that has to be administered is too high for practical clinical applications.[19] Iron oxide NPs are particularly well-suited for this application, for they have already been approved for human use as MRI contrast agents and as iron supplements.[20] This is because they have excellent biodegradability *in vivo*, with the iron from NPs metabolized and incorporated into the body's iron store.[21–23] However, the need for high NP concentrations is also a challenge, leading to efforts to synthetically enhance the magnetic properties of iron oxide NPs to optimize their tracking by MRI.[24,25] Imaging aside, iron oxide NPs offer innovative options to harness

have shown that the interaction of phagocytes with iron oxide NPs such as ferumoxytol can lead to tumour growth inhibition.[26] Furthermore, MNPs provide also possibilities for introducing new mechanisms for controlling the release, cellular fate, and biodistribution of these drugs using external magnetic stimulated manipulations such as magnetic field guided localization and hyperthermia to enhance delivery and/or combined therapeutic effects. Although none of these mechanisms have been exploited in cancer immunotherapy and in this study, a growing number of reports are providing experimental demonstration of the potential of these magnetism-based mechanisms for precision drug delivery and combinatorial therapy in chemotherapy.[27]

For effective use of MNPs in cancer immunotherapy there is considerable potential in targeting antigen presenting cells (APCs) such as macrophages and dendritic cells (DCs).[28] DCs in particular represent an ideal target because they reside in peripheral tissues and in lymph nodes (LNs), where they act as sentinels and serve as pivotal bridge between innate and adaptive immunological responses.[29] Many of these responses are triggered by recognition of specific molecules by TLRs on DCs.[30–33] Hence, TLR ligands (agonists and antagonists) are increasingly being used in the development and engineering of synthetic vaccines to combat infectious diseases and cancer.[34]-[35] However, a view that is emerging from systems biology approaches to study innate immunity is that precise spatial and temporal control of the immune responses is critically important. In particular, the cellular localization of TLR receptors has important consequences for ligand accessibility and can also have an effect on the downstream signaling events regulating the immune response.[36] Moreover, it has been shown that although TLR agonists individually may be overlooked at certain low doses, the host appears to have evolved to recognize some of these ligands together as a combinatorial assault which triggers

the potential threat, preventing a considerable infection (or potentially a tumour) from being established. Among all the TLRs, those involved in the recognition of nucleic acids such as TLR3 and TLR7 are localized within endolysosomal compartments and have been shown to synergize,[41] making them ideal for targeting through NP delivery. Even as single adjuvants, TLR3 and TLR7 agonists are included in the National Cancer Institute's ranking of immunotherapeutic agents with the highest potential to boost cancer immunotherapy outcomes.[42] Apart from targeted delivery of TLR agonists to DCs,[43] underlying the current difficulty to achieve effective antitumour responses are cancer cells expressing suboptimal tumour antigen levels.[44] The problem may be overcome if the NP also delivers tumour antigen to the LN-resident DCs so that they can activate and properly present antigen to T-cells to trigger a high-avidity antitumour response. However, tumours can actively suppress the tumour-directed cytotoxic T-lymphocyte (CTL) function expressing the transmembrane protein PD-L1, which upon binding to PD-1 expressed on the surface of activated CTLs turns off the activated lymphocytes.[45,46] Against this, one strategy would be to generate or enhance existing tumour-specific $CD8^+$ T-cell responses via the combinatorial use of particle-delivery of TLR agonists and tumour antigen and antibodies that block the PD-L1/PD-1 T-cell inhibitory interactions (i.e., immune checkpoint blockade).

In order to enhance the antigenicity, immunogenicity and efficacy of the particle-based vaccine, circumstantial evidence suggests it might be important to exploit both slow and fast delivery of adjuvant and antigen to the target cells using both small and large particles. Studies have shown that although NP-enabled direct and quick delivery of vaccine components to DCs in the draining LNs is beneficial,[12,47] rapid cell uptake or clearance from the administration site

are sustained for several days and that the slow wave of antigen-bearing DCs moving from the skin to the LNs is also required to induce full-fledge effector responses.[40,48–50] Moreover, microparticles carrying the synthetic TLR3 agonist polyinosinic-polycytidylic acid (polyIC) proved to be more immunogenic than nanoparticles when injected intranodally[51] for their ability to form an extracellular depot that confers sustained released and prolonged exposure of the TLR3 agonist in the lymphoid tissue.

Here, we set out to investigate and enhance the antitumour efficacy of TLR agonist treatments combining polyIC with the TLR7 agonist imiquimod (R837) using a versatile and easy to construct micellar MNP-based drug delivery system along with immune checkpoint abrogation at the level of the cancer cells (**Scheme 1**). In this new vaccine delivery system we incorporate small (5 nm) $Zn_xFe_{3-x}O_4$ NPs, which creates the opportunity for non-invasive vaccine localization *in vivo*. We first optimize and significantly increase the overall magnetization of the $Zn_xFe_{3-x}O_4$ NPs by zinc(II) doping, improving the spin–spin relaxation rate (R2), hence the MRI detection sensitivity of the vaccine delivery vehicles by three to four times. Next, we show that polyIC and imiquimod form polyIC-R837 complexes with R837 intercalation into the polyIC dsRNA structure, which provide synergistic and complementary antitumour effects linked to enhanced activation of antigen presenting cells and direct cancer cell killing. We finally develop and test the MNP-filled micellar system biofunctionalized with polyIC-R837 complexes and the model tumour antigen ovalbumin (OVA), with the hypothesis that it would confer both fast and sustained delivery of this cargo from the subcutaneous injection site to lymphoid tissue and tumour due to the different tendency shown to aggregate depending on the surface biofunctionalization. The results show that the combination of polyIC and R837 creates a very

protective antitumour immunity against the highly aggressive B16-F10(OVA) melanoma challenge, despite its high expression of immune inhibitory PD-L1. Moreover, we show that the antitumour immunity is improved by the MNP-filled micellar system and by prevention of PD-L1/PD-1 T-cell inhibitory interactions, for which we generated a B16-F10 melanoma cell line with silenced PD-L1. Finally, we could detect differences in the migration of the polyIC-R837- and OVA-carrying MNP-filled micelles combining MR and SPECT/CT imaging thanks to the significantly increased overall magnetization and high affinity of the MNP micelle core for ^{67}Ga radionuclide. Our results highlight the promising possibility of using polyIC-R837 complexes, micellar MNP-based drug delivery systems and checkpoint inhibition to generate protective antitumour responses as a broadly applicable, versatile and effective strategy for cancer immunotherapy, in particular when they are combined. These results along with the simplicity and versatility of the system provide an excellent framework for future clinical translation.

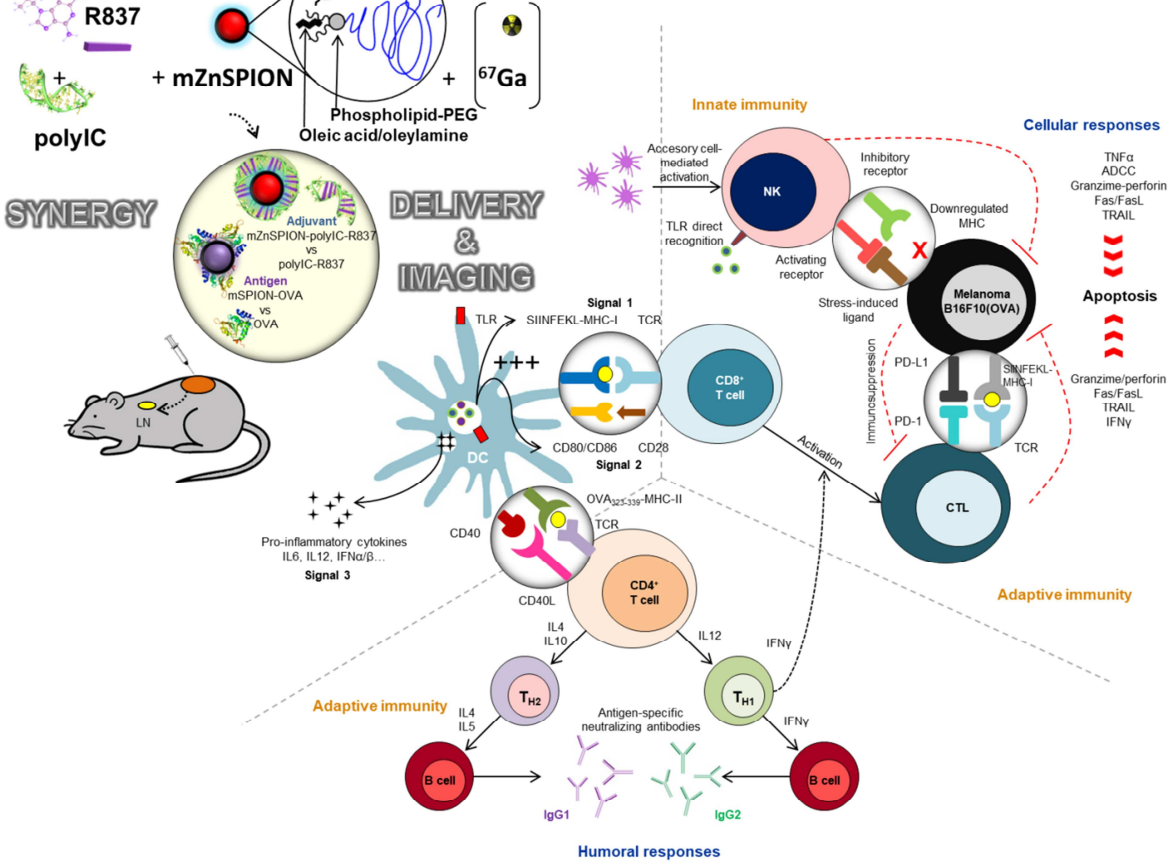

Scheme 1. Self-assembly achieved by simple physical mixture of the vaccine and nanovaccine components promotes effective drug synergy, delivery and imaging. Adjuvant and tumour antigen uptake by DCs at site of injection and/or via direct trafficking to LNs is able to activate potent and long lasting immunity against the B16-F10(OVA) melanoma cells, in particular when the expression of PD-L1 is downregulated.

Results

Synthesis and characterization of PEGylated phospholipid-encapsulated $Zn_xFe_{3-x}O_4$ NPs: mZnSPION and mSPION. Small (5 nm) magnetite and zinc-doped magnetic nanoparticles ($Zn_xFe_{3-x}O_4$ MNPs, ZnSPION) were prepared leveraging the need for high MR contrast for tracking with a desirable pathway for MNP removal,[52,53] after they have coordinated the antitumour immune responses. TEM images of the prepared hydrophobic Fe_3O_4 MNPs (SPION)

ICP-OES analyses were carried out on the ZnSPION to obtain an unambiguous determination of the level of Zn^{2+} incorporation into the spinel structure. The yielded composition of the ZnSPION used in this study, obtained using a ratio of Zn/Fe precursors of 0.21, was $Zn_{0.5}Fe_{2.5}O_4$. Thus, the applied synthetic methodology provided both excellent control of composition and particle size.

To study the changes, elemental makeup and the oxidation states on the surface brought about by zinc doping, high-resolution X-ray photoelectron spectroscopy (XPS) analyses were performed on the Fe 2p, Fe 3p, Zn 2p and O 1s regions of the Fe_3O_4 and $Zn_{0.5}Fe_{2.5}O_4$ MNPs (**Fig. S2**). The XPS spectra of the Fe 2p region show all the characteristic features of iron oxides with a mixture of Fe^{2+} and Fe^{3+} present in their structures, such as a Fe $2p_{3/2}$ peak with a binding energy of 710.60 eV and satellite shake-up peaks at higher binding energies (**Fig. S2a**).[54] The presence of Fe^{2+} and Fe^{3+} ions was confirmed through curve fitting of the Fe 3p peaks, which could be de-convoluted into two sub-peaks at 55.6 eV and 53.9/54.0 eV assigned to Fe^{3+} and Fe^{2+} ions,[55] respectively for the SPION/ZnSPION (**Fig. S2b**). In the SPION the distribution between tetrahedral (A) and octahedral (B) sites is Fe^{2+} (B site):Fe^{3+} (A site):Fe^{3+} (B site) in a ratio of 1:1:1. Several studies have shown that in these nonstoichiometric zinc-doped MNPs the Zn^{2+} ions are incorporated at the A sites but not exclusively – there is also substitution of Zn^{2+} into the octahedral sites in place of Fe^{2+} (B site).[56] This appears to agree with the results of the present study. The XPS spectra of the Fe 3p peak could be fitted to a Fe^{3+}/Fe^{2+} ratio of 2.2 and 3.5 for the Fe_3O_4 and $Zn_{0.5}Fe_{2.5}O_4$ MNPs (**Fig. S2b**), respectively. These ratios are in good agreement with the structures of these nanomaterials in which a small proportion of Fe_3O_4 MNPs have been oxidized to Fe_2O_3. The higher Fe^{3+} content of the ZnSPION is consistent with Fe^{3+} by Zn^{2+}

one Fe^{2+} ion needs to oxidize to Fe^{3+} increasing the Fe^{3+}/Fe^{2+} ratio. The two peaks with binding energies of 1021.4 eV and of 1044.4 eV (**Fig. S2c**), can be attributed to Zn $2p_{3/2}$ and Zn $2p_{1/2}$, respectively.[57] Identification of the zinc oxidation state was possible by using the modified Auger parameter, α´, defined as the difference between the kinetic energies of the most intense photoelectron ($2p_{3/2}$) and Auger (Zn $L_3M_{45}M_{45}$) peaks plus the energy of the excitation source (1486.6 eV for Al Kα). This calculation confirmed that zinc is in the 2^+ oxidation state. The high-resolution XPS spectrum for the O 1s region showed a broad asymmetric curve, which can be de-convoluted into two well-defined peaks at binding energy of 532.1 and 530.1 eV (**Fig. S2d**). The peak at 530.1 eV is characteristic of the metal–oxygen–metal (M–O–M) lattice, whilst the peak at 532.1 eV has been reported to indicate the presence of other oxygen species (*i.e.*, OH, H_2O or carboxylate species) and/or defect sites with low oxygen coordination in $Zn_xFe_{3-x}O_4$ systems.[57]

The motivation for doping magnetite NPs with Zn^{2+} ions was to improve the magnetic properties for biomedical applications. The magnetization (*M*) versus applied magnetic field (H) of the MNPs was measured at 5 K and 293 K (**Fig. 1a,b**). The MNPs exhibit superparamagnetic behavior without hysteresis and remanence at 293 K and ferromagnetic behavior with a coercivity (H_c, the applied field required to reverse magnetization direction) of 51 Oe (Fe_3O_4) and 178 Oe ($Zn_{0.5}Fe_{2.5}O_4$) at 5 K. Most biomedical applications of MNPs benefit from high saturation magnetization (M_s) values. The M_s of the prepared SPION and ZnSPION is 55 emu g^{-1} and 76 emu g^{-1} respectively at 293 K, among the highest for this particular MNP size. It has been shown that higher magnetization of this type of zinc-doped MNPs arises from the partial substitution of Fe^{3+} cations at A sites by non-magnetic atoms such as Zn^{2+}, which results in an

Fe^{3+} ions at A and B sites. Since this effect is seen to increase only up to a certain percentage of zinc (< 20 % of the total transition metal),[56] the prepared $Zn_{0.5}Fe_{2.5}O_4$ ZnSPION can be considered of very high quality and optimum for enhanced MRI, where a high mass magnetization value typically leads to enhanced MRI sensitivity (*vide infra*).

Stable and water soluble micelles with encapsulated Fe_3O_4 or $Zn_{0.5}Fe_{2.5}O_4$ MNPs inside (mSPION or mZnSPION) were prepared by self-assembly of commercially available PEGylated phospholipids (1,2-dipalmitoyl-sn-glycero-3-phosphoetanolamine-N-[methoxy(polyethylene glycol)-2000) around the hydrophobic iron oxide NPs. Dynamic light scattering (DLS) studies show that mSPION and mZnSPION have very similar sizes with average hydrodynamic diameters below 50 nm (**Fig. 1c** and **Fig. S3**).

To elucidate the extent to which the Zn-doped MNPs provide enhanced performance as MR imaging contrast agents compared to the magnetite NPs, we measured the longitudinal relaxation time (T_1) and transverse relaxation time (T_2) for mSPION and mZnSPION at 1.5 Tesla (T) on a Bruker Minispec relaxometer. The longitudinal relaxivity (r_1) and transverse relaxivity (r_2) values were determined by calculating the slope of a plot of the inverse relaxation time against the iron concentration. Consistent with the magnetization results, mZnSPION showed the strongest MR contrast effect, with a relaxivity r_2 value of 115.06 ± 17.46 mM^{-1} s^{-1}, more than 3 times larger than for mSPION (31.06 ± 5.39 mM^{-1} s^{-1}).

The contrast enhancement efficacy of the magnetic nanoconstructs was also tested in a 7 T pre-clinical MRI scanner. The phantom images showed that the magnetic nanovaccine delivery vehicles are effective contrast agents under the settings for the preclinical *in vivo* imaging studies (*vide infra*), and that mZnSPION demonstrate superior performance (**Fig. 1d**). Moreover, both

agents at higher field strengths.

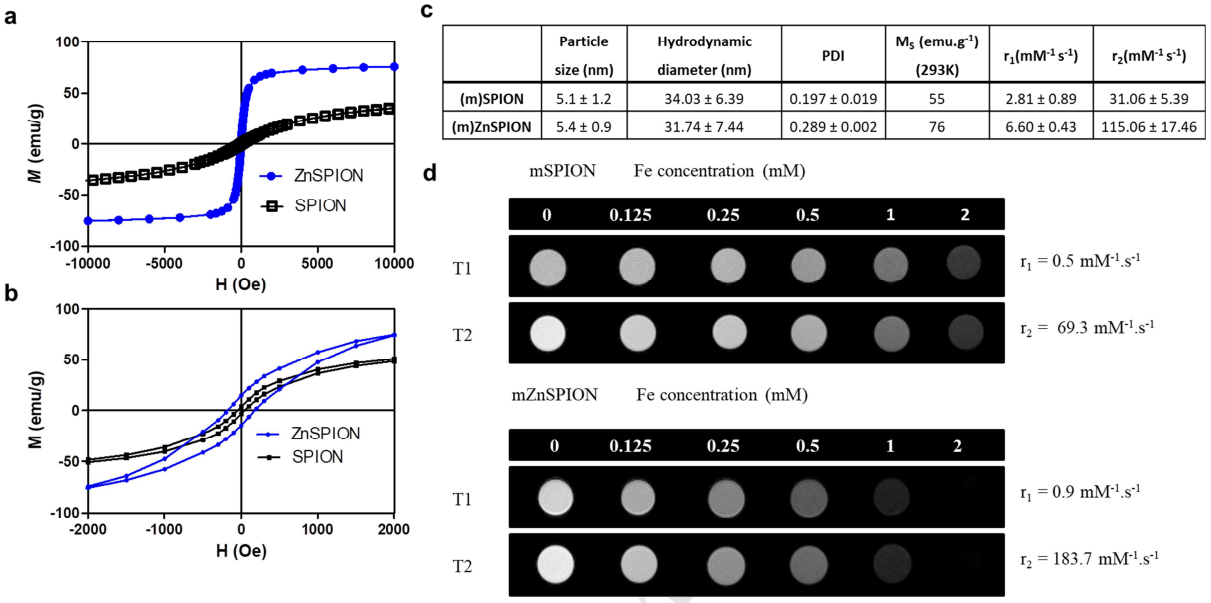

	Particle size (nm)	Hydrodynamic diameter (nm)	PDI	M_S (emu.g^{-1}) (293K)	r_1(mM^{-1} s^{-1})	r_2(mM^{-1} s^{-1})
(m)SPION	5.1 ± 1.2	34.03 ± 6.39	0.197 ± 0.019	55	2.81 ± 0.89	31.06 ± 5.39
(m)ZnSPION	5.4 ± 0.9	31.74 ± 7.44	0.289 ± 0.002	76	6.60 ± 0.43	115.06 ± 17.46

Fig. 1. Magnetic properties, MR relaxivities and MR imaging. Magnetization (M-H) curves of the prepared SPION and ZnSPION at: (a) 293 K and (b) 5 K (magnified view). (c) Summary of size and magnetic properties (longitudinal (r_1) and transversal (r_2) relaxivity values obtained at 1.5 T). (d) T_1 and T_2-weighted phantom MR images of mSPION and mZnSPION dispersed in 2 % agar obtained using a 7 T preclinical MR scanner with the determined relaxivity values.

Double-functionalization of mZnSPION with polyIC and R837. It is emerging that some TLRs cooperate with each other to be more effective detecting imminent infection or danger and triggering protective immune responses, so we focused on the development of nanoconstructs carrying two TLR ligands as adjuvants. Recently, we reported that the TLR3 agonist polyIC can be incorporated non-covalently to mSPION to provide enhanced immune responses.[58] Since imidazoquinolines can intercalate into the double-stranded structure of nucleic acids,[59] we envisaged that using a polyIC coated mZnSPION would achieve co-delivery of polyIC and R837 by complexing R837 molecules to polyIC. After overnight incubation of polyIC with

(MWCO 100 kDa) centrifugal device to remove unbound polyIC molecules. The mZnSPION-polyIC showed the UV absorption peaks at 245 nm and 267 nm characteristic of poly (I:C) (data not shown). The amount of polyIC decorating the mZnSPION surface was quantified by measuring the absorbance at 260 nm after hydrolysis overnight with 0.2 N NaOH, ultracentrifugation (369,000 × g, 40 min) to remove the digested nanoparticles and comparison to a standard curve of polyIC treated in the same way.

R837 presents fluorescence emission λ_{max} at 338 and 354 nm using an excitation wavelength of 250 nm. To elucidate if the imidazoquinoline molecules associate with polyIC the fluorescence spectra of R837 was recorded in the presence of increasing amounts of polyIC, showing significant fluorescence quenching like upon intercalation of other organic dye molecules into dsDNA (**Fig. S4a**). We reasoned that potentially, R837 could also be coordinated to unsaturated metal sites on the iron oxide surface. By alternating the order of addition of each TLR agonist, however, we found that the presence of the nucleic acid was critical for incorporating the imidazoquinoline molecules into the NP system. When R837 is added to the mZnSPION-polyIC complexes and excess R837 is removed by three cycles of ultrafiltration, the amount bound to the mZnSPION-polyIC complexes could be quantified analyzing a characteristic peak of R837 at 320 nm by UV spectroscopy (**Fig. S4b**) and comparing with a calibration curve for R837. By contrast, when R837 was added first to the mZnSPION micelles and then polyIC, only the presence of polyIC could be detected (data not shown). Once the amount of R837 was estimated, solutions containing free R837 + polyIC (polyIC titrated into the solution of R837) were analyzed by UV-vis and compared against mZnSPION-polyIC-R837 – mZnSPION at the same iron concentration determined by ICP-OES to ensure that vaccines and nanovaccines had the

increased the size of the micelles and led to the appearance of some aggregates, which were clearly detected both by DLS and TEM (**Fig. S5a-c**). As expected from the presence of the negatively charged polyIC molecules on the micelle surface, the zeta potential of the mZnSPION-polyIC-R837 was more negative than for the parent mZnSPION (- 20.2 ± 1.59 mV *vs* - 6.3 ± 0.95 mV) (**Fig. S5d**). To study the stability of the system and release of polyIC and R837, we measured the size and zeta potential of the prepared mZnSPION-polyIC-R837 immediately after purification and one week later, in 10 mM PBS for size measurements and in NaCl 0.09 % for zeta potential. The size and negative zeta potential of the functionalized micelles did not change significantly, which is consistent with retention of polyIC on the surface of mZnSPION (**Fig. S6**). To study the release of R837, at designed time points 10 mM PBS solutions of mZnSPION-polyIC-R837 were subjected to ultrafiltration using a NanoSep 100k (MWCO 100 kDa) centrifugal device and the UV-vis spectra of the retentate and filtrate recovered from each device was measured to quantify the fraction of released R837. Analyzing the absorbance at 320 nm shows the release of R837 (**Fig. S7**).

mZnSPION-polyIC-R837 complexes are effectively internalized and localize within the target endosomal compartments of antigen presenting cells. The uptake and fate of mZnSPION-polyIC-R837 complexes incorporating rhodamine B-modified DPPE phospholipid (< 5 %), was analyzed by fluorescence microscopy. LysoTracker Green was used to selectively stain late endosomes and lysosomes. Live cell microscopy studies showed that after 1 h incubation mZnSPION-polyIC-R837 complexes are co-localized with LysoTracker (**Fig. S8a**). This is an important result because it is widely accepted that TLR3 and TLR7 localize to and

TLR7 to co-localize with TLR3-containing compartments.[61] Flow cytometry studies showed that the cellular uptake of mZnSPION-polyIC-R837 is quite fast, being taken up by macrophages even after 1 h exposure (**Fig. S8b**).

Synergistic activation of antigen presenting cells and melanoma cell killing by polyIC-R837 and mZnSPION-polyIC-R837. R837 and polyIC have both generated intense interest in cancer research owing to their potent antitumoural activities, which arise from diverse and cooperative mechanisms of action.[62,63]

First, we investigated the immunostimulatory properties in the murine macrophage cell line J774A.1 and in bone marrow derived dendritic cells (BMDCs). We demonstrate a strong synergistic pro-inflammatory activation of the J774A.1 cells and of BMDCs over a range of polyIC and R837 concentrations and ratios (**Fig. S9**). However, secretion of cytokines by macrophages and DCs showed different sensitivity to stimulation with R837 and the polyIC-R837 combination. Macrophages responded less to stimulation with R837 but strongly to the co-stimulation (**Fig. S9a**). DCs became highly stimulated even with low R837 concentrations (0.5-5 µg/mL) and showed less synergistic activation by co-stimulation with the TLR3 agonist (**Fig. S9b**).

Next, BMDCs and J774A.1 macrophages were stimulated with the TLR agonists at fixed concentration, free and coating mZnSPION, singly and combined (**Fig. 2**). In macrophages, stimulation with polyIC-R837 and mZnSPION-polyIC-R837 synergistically enhanced IL-6 production to a similar extent (**Fig. 2a**). In contrast, release of pro-inflammatory IL-6 and IL-12

R837 complexes compared with the free TLR agonists (**Fig. 2b**). Although mZnSPION showed slightly higher toxicity than mSPION (**Fig. 2c**), the mZnSPION did not alter the viability of macrophages and BMDCs at the concentrations used for cell activation (iron concentrations < 0.15 mM Fe). The enhanced activity of mZnSPION-polyIC-R837 compared to free polyIC-R837 is also reflected in its cytotoxicity (**Fig. 2d**). To test whether delivery by mZnSPION also affected BMDC maturation, we analyzed the surface expression of co-stimulatory molecules and maturation receptors (CD80, CD86 and CCR7) (**Fig. 2e**). Increased expression of the co-stimulatory molecules CD80 and CD86 is required for full activation of T-cells and induction of anti-tumour T-cell functions.[64] DCs co-stimulated with free polyIC and R837 and mZnSPION-polyIC-R837 complexes showed comparable high expression levels of CD80 and CD86. Stimulation with uncoated mZnSPION resulted in baseline activation levels equal to those observed in untreated BMDCs. By contrast, the expression levels of the chemokine receptor CCR7 which regulates cell migration[65] was lower in BMDCs stimulated with mZnSPION-polyIC-R837 complexes than in those stimulated with free polyIC-R837. Although the link between TLR signaling and zinc homeostasis has not been fully investigated, this result seems consistent with previous studies suggesting that increase in free zinc in DCs is involved in at least some DC maturation events and may affect the magnitude of adaptive immune responses.[66]

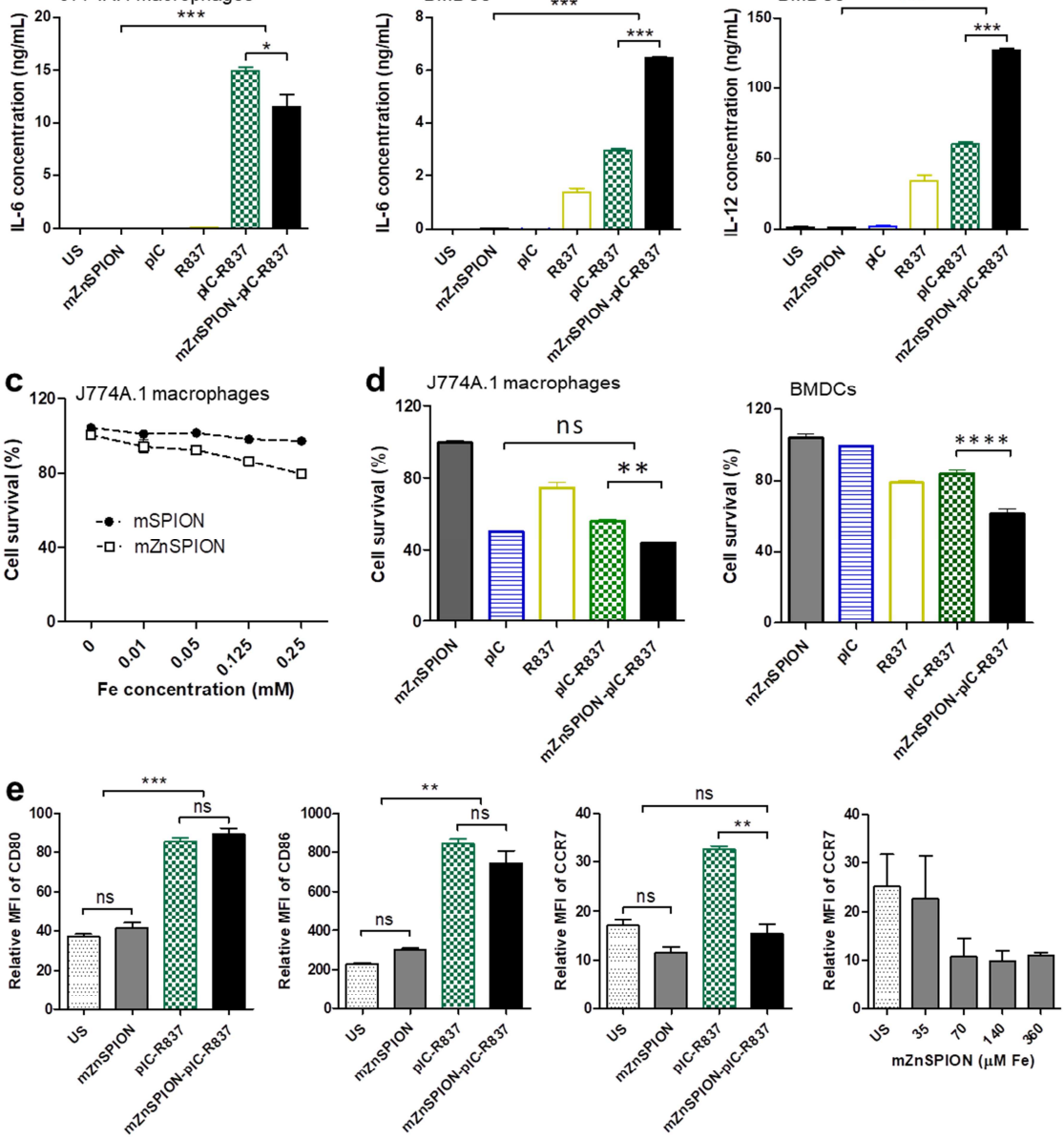

Fig. 2. mZnSPION-polyIC-R837 enhances immunostimulatory functions in macrophages and DCs compared to polyIC-R837. J774A.1 macrophages and BMDCs were incubated for 24 h with the indicated formulations. Cytokine release in (a) J774A.1 macrophages and (b) BMDCs. (c) Analysis of the cytotoxicity of mSPION and mZnSPION in J774A.1 macrophages. (d) Cell viability of J774A.1 macrophages and BMDCs. (e) Relative expression levels of maturation markers (CD80, CD86 and CCR7) expressed as the mean fluorescence intensity of each marker in BMDCs ($CD11c^+$ $MHC\text{-}II^+$ cells). Data are representative of three independent experiments. ****P<0.0001, ***P<0.001, **P<0.01, *P<0.05, ns = non significant by one-way ANOVA followed by Tukey's test.

DCs, for which studying immunostimulatory functions is of special relevance, R837 and polyIC can exert additional effects against tumour cells.[62,67–69] To investigate the potential direct killing of the cancer cells, B16-F10(OVA) cells were incubated with different concentrations of polyIC, R837 and combinations of polyIC and R837 for 24 h, 48 h and 72 h. The results showed that only R837 has the ability to kill the B16-F10(OVA) melanoma cells. Moreover, the combinations of polyIC and R837 afforded cytotoxicity profiles comparable to those of R837 alone (**Fig. S10**). These results suggest that 'off-target' R837 molecules interacting with B16-F10(OVA) melanoma cells can potentially contribute to the overall antitumoural activity. Hence, this system unfolds as highly attractive for reinforcing antitumour responses through encounters with both immune cells and cancer cells.

Immunization with polyIC-R837 drives effective immune responses which are enhanced by the mZnSPION and mSPION delivery vehicles. Clinical use of TLR agonists has been limited mainly by difficulties to restrict their systemic distribution and toxicity due to off-target activity.[34] To study the adjuvanticity, efficacy and *in vivo* effects of polyIC-R837, C57BL/6 mice were immunized in the hind hock (lateral tarsal region just above the ankle) with low doses of these adjuvants (3 µg polyIC/mouse, 1 µg R837/mouse) free and complexed to mZnSPION (5 µg mZnSPION/mouse). We observed minimal systemic production of IL-6 (**Fig. 3a**). By contrast, 24 h after immunization, both polyIC-R837 and mZnSPION-polyIC-R837 were able to activate DCs and NKs in the spleen and draining LNs (**Fig. 3b, c**).

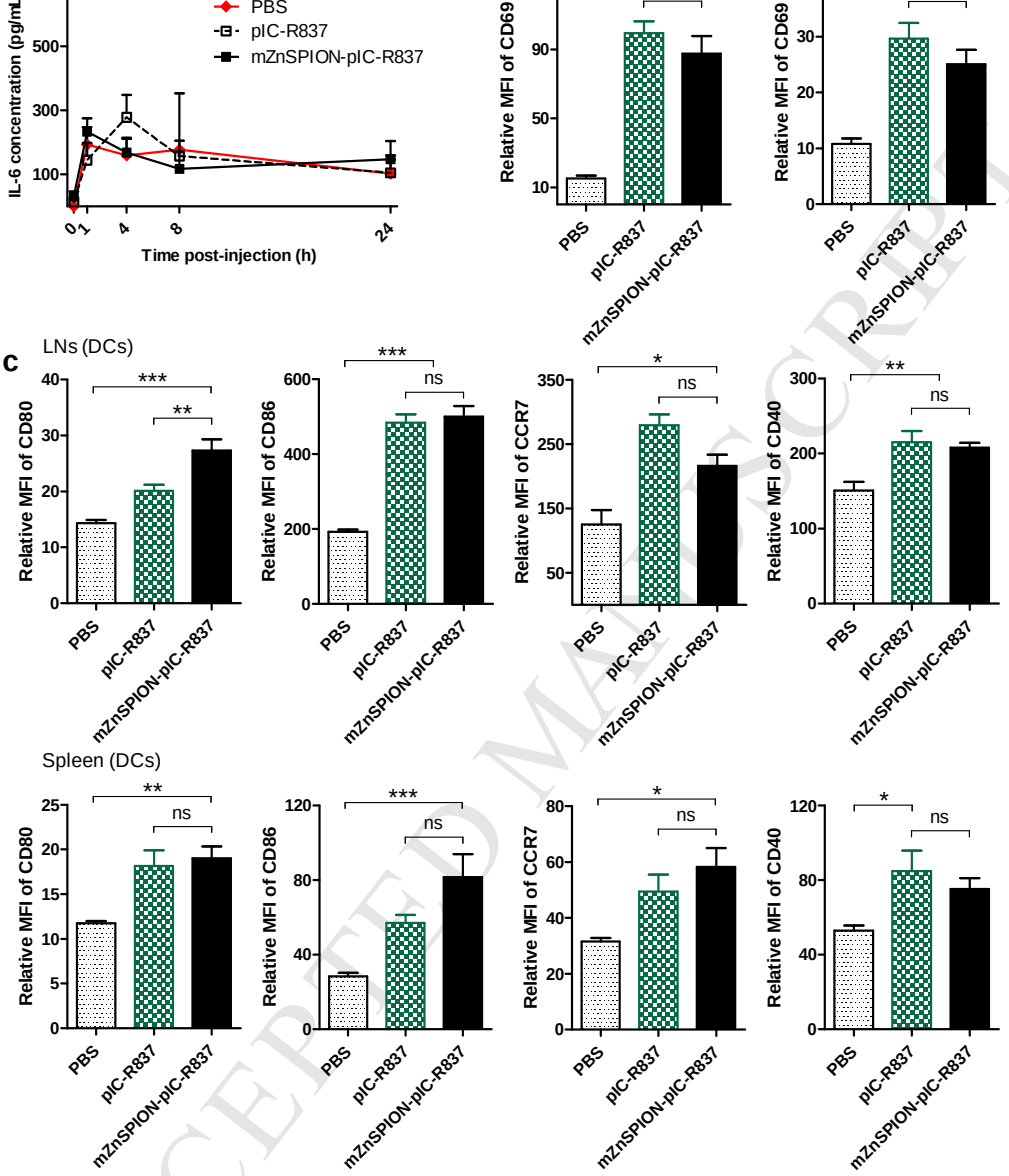

Fig. 3. Innate immune responses triggered by low doses of polyIC-R837 and mZnSPION-polyIC-R837 (3 µg polyIC, 1 µg R837 and 5 µg mZnSPION per mouse). (a) IL-6 levels in blood. (b) Relative mean fluorescence intensity histograms of CD69 natural killer cells ($CD3^-$ $Nkp46^+$) maturation marker, extracted from inguinal and popliteal LNs and spleen of mice 24 hours after immunization. (c) CD80, CD86, CD40 and CCR7 relative mean fluorescence intensity histograms of $CD11c^+$ $MHC\text{-}II^+$ dendritic cells extracted from inguinal and popliteal LNs and spleen of mice 24 hours after immunization. Data are mean ± SEM (n = 5 mice per group). $^{***}P<0.001$, $^{**}P<0.01$, $^{*}P<0.05$, ns = non-significant by one-way ANOVA followed by Tukey's test.

and significantly improves adaptive immune responses compared to administration of free OVA.[70] In the present study, we assessed the effect of co-administration of mZnSPION-polyIC-R837 adjuvant and mSPION-OVA. In these studies, mice were immunized twice (day 0 and 14) with low doses of antigen (5 µg of OVA/mouse) and adjuvant (< 4 µg/mouse). The production of OVA-specific IgG, IgG1 and IgG2c antibodies in blood sera collected on days 0, 14, 28 and 35 was evaluated by ELISA. On day 14, mice treated with mSPION-OVA and mZnSPION-polyIC-R837 already showed the highest levels of total IgG and IgG1 antibodies, and OVA-specific IgG2c titers increased by more than two log orders compared to mice treated with the nanoparticle-free vaccines (**Fig. 4a**). Thus, the polyIC-R837 adjuvant and OVA administered by the mZnSPION and mSPION vehicles elicited a more balanced Th1/Th2 response enhancing both IgG1 and IgG2c titers. This is relevant since IgG2 antibody isotypes have been implicated in enhanced protection in both infectious diseases and cancer.[71]

Moreover, the results showed that the combination of polyIC with R837 acts as a potent adjuvant, as the total IgG, IgG1 and, in particular, IgG2c titers were significantly increased with respect to vaccination with OVA alone (100 to 1000-fold) when OVA or mSPION-OVA were co-administered with polyIC-R837 or mZnSPION-polyIC-R837 complexes. In addition, compared with our recently developed mSPION-CpG adjuvant system,[70] which was tested under identical experimental conditions and significantly enhanced the adjuvanticity of CpG, immunization with polyIC-R837 (and even more so with mZnSPION) led to higher OVA-specific antibody titers, further demonstrating the strong adjuvanticity of this specific combination of TLR agonists.

able to drive antigen-specific $CD8^+$ T-cell responses in mice, comparing the magnitude of this response against the simple mixtures (OVA + polyIC-R837). Each week we monitored the frequency of $OVA_{257-264}$ (SIINFEKL)-specific $CD8^+$ T-cells by H-2Kb/SIINFEKL dextramer staining and flow cytometric analysis. After 7 days, mice immunized with mZnSPION-polyIC-R837 and mSPION-OVA exhibited the highest frequency of circulating SIINFEKL-specific $CD8^+$ T-cells in the blood (**Fig. 4b**). As can be expected, these levels were lower on day 14, but remained higher for the mice immunized with mZnSPION-polyIC-R837 and mSPION-OVA. On day 35 (experimental end point), the frequencies of circulating OVA-specific $CD8^+$ T-cells in peripheral blood, spleen and draining LNs were similar for mice immunized with OVA + polyIC-R837 and mSPION-OVA + mZnSPION-polyIC-R837 (**Fig. 4c**). Taken together, these results demonstrate that combination of polyIC and R837 is a robust and effective adjuvant inducing both cellular and humoral immune responses at very low doses following a prime-boost regimen. In addition, it avoids a strong and potentially harmful systemic inflammatory response, and its efficacy is significantly enhanced by the mZnSPION system.

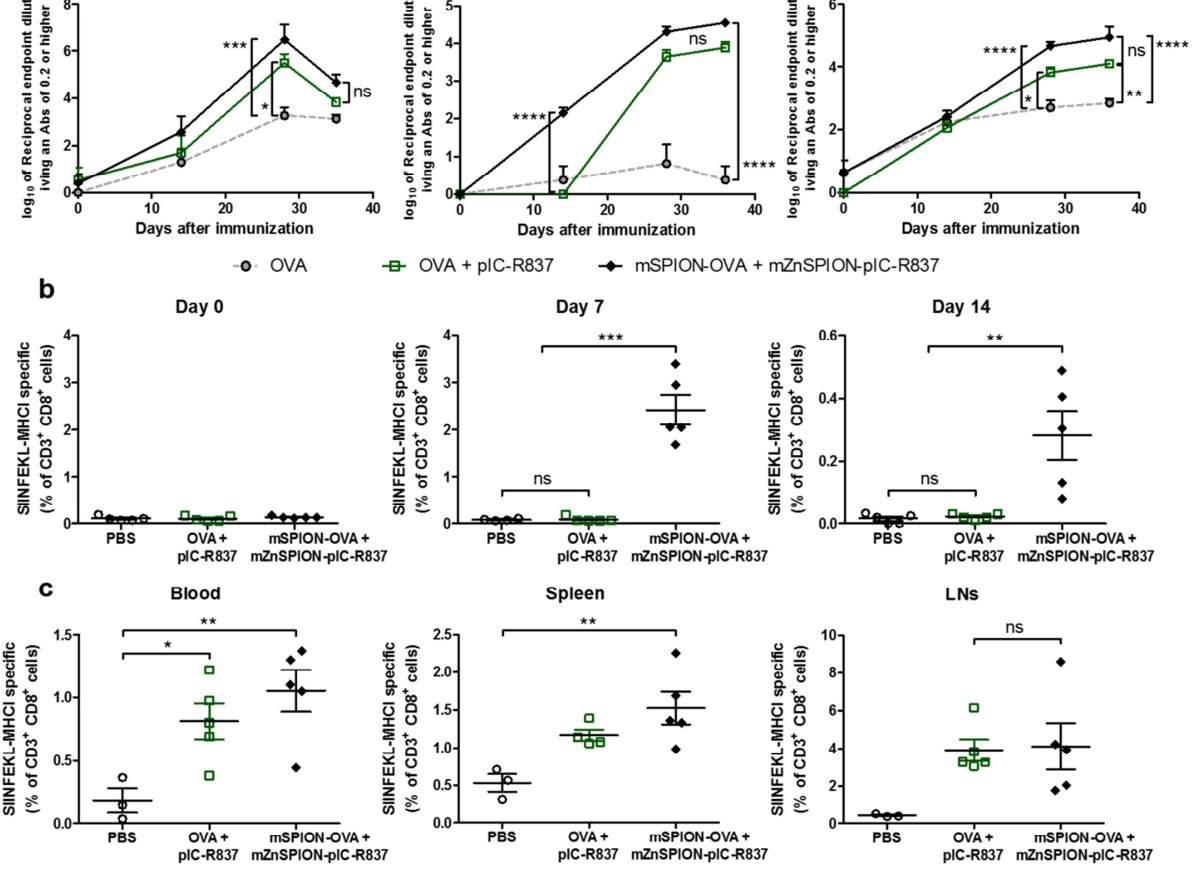

Fig. 4. Immunization with mZnSPION-polyIC-R837 and mSPION-OVA enhances humoral and cellular immune responses. C57BL/6 mice were s.c. immunized into the flanks with the indicated formulations on day 0 (prime) and 14 (boost) (5 μg of OVA, 4 μg of polyIC, 0.5 μg of R837, 12 μg mZnSPION and 45.5 μg SPION per mouse). (a) OVA-specific serum IgG1, IgG2c and total IgG titers. Analysis of frequency of circulating $OVA_{257-264}$ (SIINFEKL)-specific $CD8^+$ T-cells isolated from (b) blood at different time points and (c) blood, spleen and inguinal LNs at day 35 after first immunization. Data presented as mean ± SEM. n = 5 mice per group. ****P<0.0001, ***P<0.001, **P<0.01, *P<0.05, ns = non significant by (a) two-way ANOVA followed by Bonferroni's test and (b, c) one-way ANOVA followed by Tukey's test.

using the mZnSPION and mSPION vehicles and by prevention of PD-L1/PD-1 T-cell inhibitory interactions. Considering the very encouraging development of potent cellular and humoral responses using small drug and nanoparticle doses, we next evaluated the efficacy of the vaccines and nanovaccines in the syngeneic melanoma model with the B16-F10 melanoma cells expressing OVA. This tumour model is highly aggressive and poorly immunogenic but susceptible to be recognized and killed by high avidity $OVA_{257-264}$ (SIINFEKL)-specific $CD8^+$ T-cells.[72] Mice were s.c. immunized on days 0 and 14 with the different vaccines. On day 21, mice were challenged with 3×10^5 B16-F10(OVA) melanoma cells and tumour growth was monitored until the tumour volume reached the limits of the established endpoint (**Fig. 5a)**. First, to determine the efficacy of the TLR3 and TLR7 agonist adjuvant combination, we compared immunization with OVA + polyIC, OVA + R837, OVA + polyIC-R837 and a control group that was immunized with 10 mM PBS. Compared to the PBS treatment, the immunization with each of TLR agonists combined with OVA significantly delayed the tumour growth (Figure 5b). Vaccination with OVA + polyIC-R837 significantly inhibited tumour growth and improved survival compared to immunization with tumour antigen and single TLR agonists at the same concentration (**Fig. 5b-f**). Strikingly, most mice immunized with OVA + polyIC-R837 remained free of visible tumour for several months post-tumour challenge despite the low doses of antigen and adjuvant administered (**Fig. 5f**). Next, we carried out studies to evaluate whether use of the nanoparticle vehicles (mZnSPION and mSPION) leads to improved anti-melanoma vaccination adopting a similar treatment schedule (**Fig. 5g**). The prophylactic effect of the vehicles alone was null. More than two months (70 days) after the last immunization mSPION-OVA combined with mZnSPION-polyIC-R837 achieved 100 % tumour rejection. Animals with a complete rejection

the left back (contralateral to the first tumour inoculation), and tumour growth was monitored on both sides. All the mice rejected the tumour re-challenge. Thus, immunizations with and without nanoparticles showed remarkable tumour protection, with many animals (100 % in the case of immunization with mSPION-OVA + mZnSPION-polyIC-R837, and 60 % in the case of OVA + polyIC-R837 immunizations) tumour-free until the end of the experiment, 115 days after the boost (**Fig. 5h, i**).

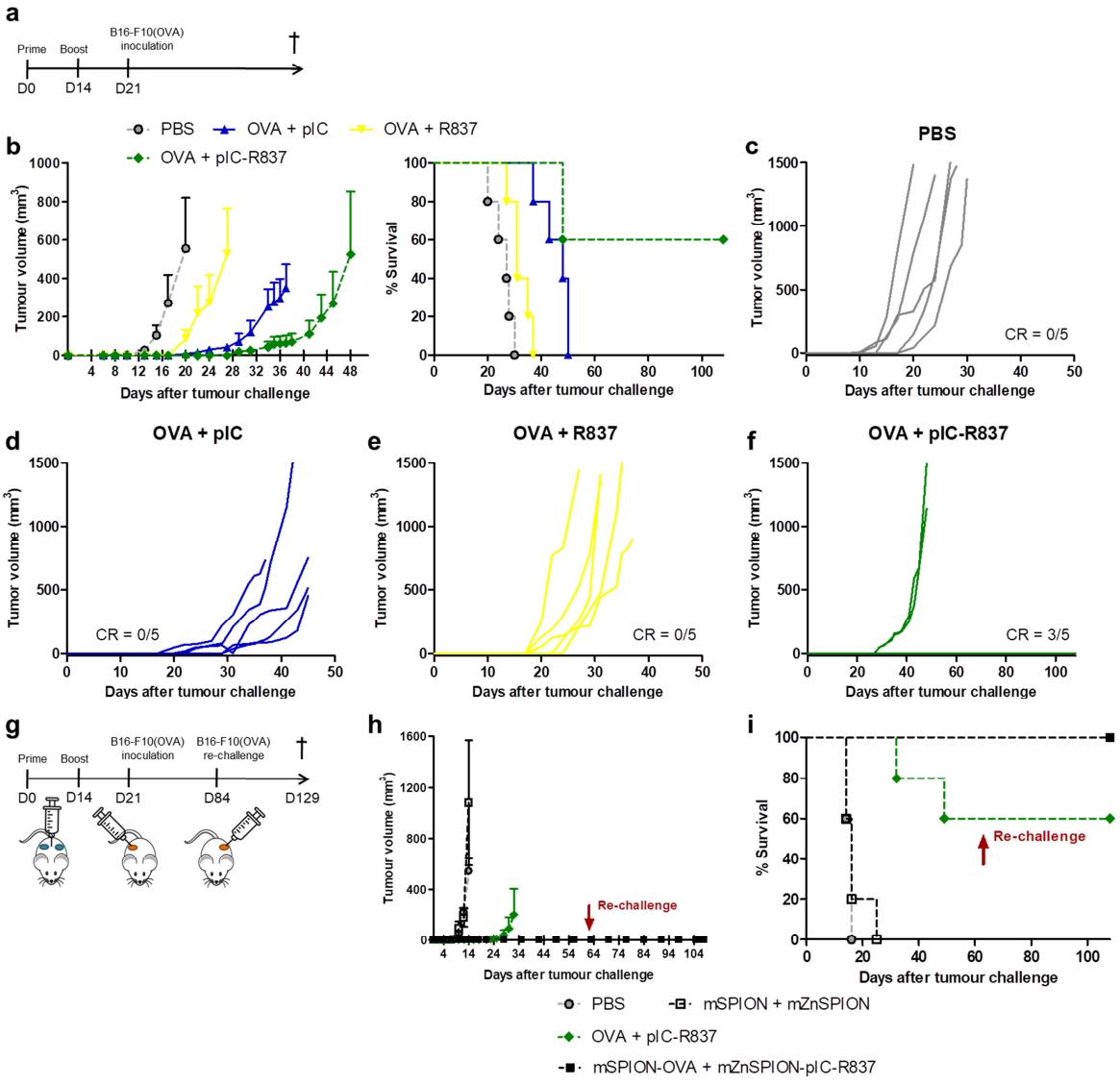

vehicles. (a) Treatment scheme. C57BL/6J mice (n = 5) were s.c. challenged with 3×10^5 B16-F10(OVA) cells/mice seven days after the last vaccination with the indicated formulations (5 µg of OVA, 4 µg of polyIC and 2 µg of R837 per mouse). (b-f) Average and individual tumour growth curves and Kaplan–Meier survival curves. (g) Treatment scheme. C57BL/6J mice (n = 5) were s.c. challenged with 3×10^5 B16-F10(OVA) cells/mice seven days and seventy days after the last vaccination with the indicated formulations (vaccines and vehicles: 5 µg of OVA, 12 µg of polyIC, 3.5 µg of R837, 10 µg mZnSPION and 55 µg mSPION; nanovaccines: mZnSPION(10 µg)-polyIC(8 µg)-R837(2.5 µg), mSPION(55 µg)-OVA(5 µg)). (i, h) Tumour growth and Kaplan–Meier survival curves. CR = fraction of complete tumour rejection.

To analyze the magnitude and quality of the memory response generated in the mice that survived free of disease until the end of the experiment (day 129), the $CD8^+$ T cell population in the spleen was analyzed. Remarkably, antigen-specific T-cells elicited by the polyIC-R837-containing vaccines persisted even 115 days after the boost. The T cell memory compartment can be subdivided into two populations, central memory $CD8^+$ T cells (T_{cm}) and effector memory (T_{em}).[73] The frequency of T_{em} and T_{cm} population was similar in the mice immunized with and without nanoparticle delivery vehicles (**Fig. S11a**). However, analysis of the T_{em} subset revealed that immunization with mZnSPION-polyIC-R837 + mSPION-OVA leads to an increased population of SIINFEKL-specific T_{em} compared to mice immunized with polyIC + R837 + OVA (Fig. S11b). To evaluate the quality of $CD8^+$ T cell responses, cellular extracts from spleen were cultured *ex vivo* and incubated with the antigenic peptide SIINFEKL for 5 h, and the IFN-γ and TNF-α intracellular production, as well as the degranulation marker CD107a, were analyzed by flow cytometry. The data demonstrated that mice immunized with the nanoparticles generate T lymphocytes with enhanced cytolytic activity (Fig. S11c,d). Taken together, these results indicate development of a potent and long lasting antitumor immunity, in which the NPs improve both the magnitude and the quality of the memory response.

treatment.[74] To date, the most effective immune checkpoint inhibitors are monoclonal antibodies that bind to either PD-1 or PD-L1.[75] The B16-F10(OVA) melanoma model used in our *in vivo* functional experiments showed a high PD-L1 basal expression (**Fig. S12**), thus indicating that this tumour model is susceptible to be rejected by PD-L1 checkpoint blockade-based treatments. Hence, we next evaluated the potential to improve the therapeutic efficacy by a combination therapy which prevents PD-L1/PD-1 T-cell inhibitory interactions.

However, there are several limitations in the use of PD-L1 blocking antibodies. The short duration of the induced responses requires successive antibody administrations for the treatment to be effective. Moreover PD-L1, is expressed on a variety of immune cellular populations, including T- and B-lymphocytes, dendritic cells, macrophages, mesenchymal stem cells, natural killer cells and bone marrow-derived mast cells,[76],[77] where blockade can result in uncontrolled auto-reactivity and significant toxicity. To overcome these limitations, we have developed a genetically modified B16-F10(OVA) cell line with a downregulated expression of PD-L1 through the CRISPR/Cas9 gene editing system delivered within lentiviral particles (**Fig. S12**).[78] This novel technology allows the permanent disruption of the target gene based uniquely on two components: a short sequence of complementary RNA to guide the recognition of the target gene and the enzyme caspase 9 for targeted DNA cleavage.[79] The use of lentivirus for its delivery enables to diminish the detrimental effects arising from the sustained expression of caspase 9.[80] Lentivirus were produced in 293T cells and purified to use them as a tool for the targeted disruption of the PD-L1 gene in B16-F10(OVA) cells *in vitro*.

immunization assay (**Fig. S13**). As expected, the permanent PD-L1 checkpoint blockade enhanced the efficacy of vaccination with OVA + polyIC-R837, with now 100 % of the animals free of tumour at the end of the experiment (115 days after the last immunization).

Finally, we carried out a preliminary study to evaluate this system in the setting of therapeutic vaccination. For this, C57BL/6 mice inoculated subcutaneously with 3×10^5 B16-F10(OVA) cells were vaccinated with OVA and polyIC-R837 free or in conjugation with the magnetic micelles on days 4, 7 and 11 and tumour growth was measured for 18 days. To compare the adjuvant effects of polyIC-R837 and nanoparticle vehicles another group of mice was treated with mZnSPION and mSPION-OVA. Results showed significant tumour growth inhibition with all three treatments. Notably, OVA + polyIC-R837 free and mZnSPION + mSPION-OVA provided comparable tumour growth inhibition, which further demonstrates the strong adjuvant effects of the nanoparticles. Treatment with mZnSPION-polyIC-R837 and mSPION-OVA provided the most potent tumour growth inhibition (**Fig. 6**). However, one week after the last treatment tumour necrosis and early ulceration signs were detected in some mice, and therefore studies to tackle control of the established tumours by multi-modal approaches are underway.

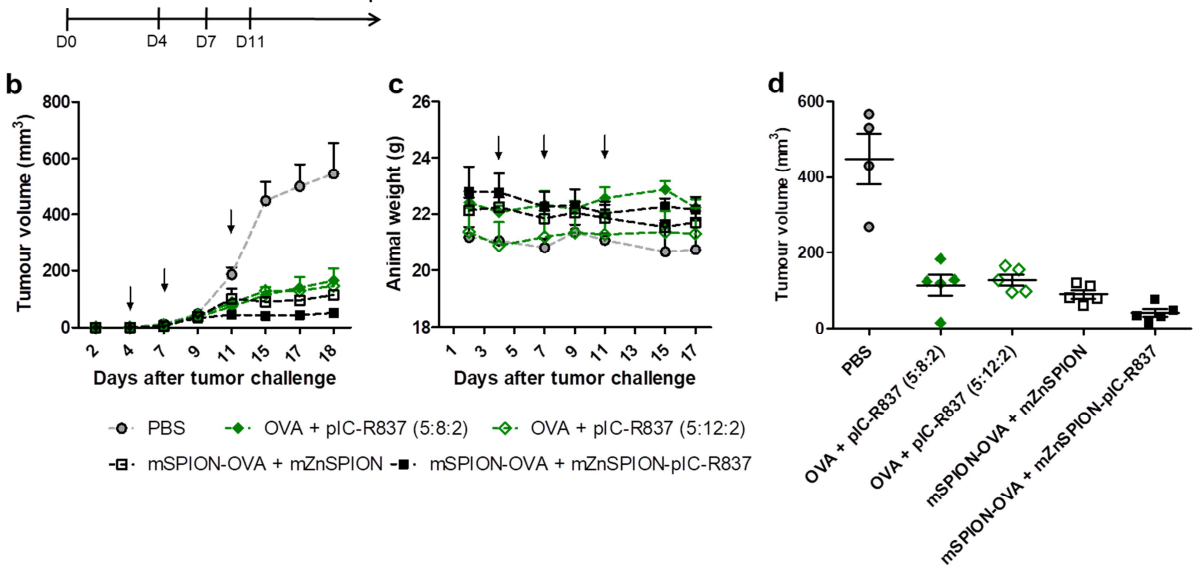

Fig. 6. mZnSPION-polyIC-R837 delays the tumour growth enhancing the efficacy of the free ligands. (a) Treatment scheme. C57BL/6J (n = 5) mice were s.c. challenged with 3 x 10^5 B16-F10(OVA cells/mice. At days 4, 7 and 11 mice were treated with TLR agonist and OVA in solution or attached to nanoparticles. (b) Curves of tumour growth, (c) animal weight over the treatment schedule, and (d) tumour volumes 15 days after the inoculation of B16-F10(OVA) cells. Arrows indicate the days of therapy administration. Doses: 5 μg of OVA, 8 or 12 μg of polyIC, 2 μg of R837; nanovaccines: 5 μg of OVA, 8 μg of polyIC, 2 μg of R837, 27 μg mSPION, 10 μg mZnSPION.

Detection of different migration of nanovaccine components to tumour and draining LNs combining MR and SPECT/CT imaging. Finally, given the excellent antitumour results obtained in response to immunization with mZnSPION-polyIC-R837 and mSPION-OVA, we studied their migration from the s.c. site of injection combining MR and SPECT/CT imaging in B16-F10(OVA) tumour bearing mice. The relaxometric studies showed that mZnSPION provides 3-4 times better sensitivity as T_2 contrast agent than the mSPION, and therefore are more suitable for MRI tracking at the low concentrations used in the immunization studies. To investigate the potential of tracking by MRI the migration of mZnSPION-polyIC-R837 from the

into C57BL/6 mice, and after tumour establishment, mZnSPION-polyIC-R837 (100 µL, [Fe] = 6 mM) was injected into the peritumoural region. MR images were acquired prior to the administration of mZnSPION-polyIC-R837 and 24 h and 48 h post-injection. Despite greatly enhanced magnetic properties, we could not detect darker signals due to migration and reduction in T_2 values in the tumour or draining LN (right inguinal LN, **Fig. 7a**). Instead, MRI showed that both 24 h and 48 h post-injection the mZnSPION-polyIC-R837 remained mainly at the injection site (**Fig. 7c**). To investigate if the polyIC-R837 coating affects the migration kinetics of the delivery vehicles, a group of mice were administered the "naked" mZnSPION. Notably, administration of "naked" mZnSPION results in reduction of T_2 values in the draining LNs 24 h post-injection (**Fig. 7b**).

Due to sensitivity limitations of MR imaging, we radiolabelled the nanovaccines with ^{67}Ga for SPECT/CT imaging. We previously demonstrated effective ^{67}Ga radiolabeling of "naked" mSPION.[70] Here, we demonstrate that zinc doping and biofunctionalization with polyIC-R837 or OVA does not affect the efficiency of radiolabeling protocol (**Fig. S14a**). We assessed the stability of the ^{67}Ga-labelled mZnSPION-polyIC-R837 by quantifying ^{67}Ga release in PBS at 37 ºC. The studies showed good stability, with less than 12 % of the bound ^{67}Ga being released over 24 h in the presence of a large excess of DOTA chelator (at DOTA:NP molar ratio of 1×10^6:1). The radiolabelled mSPION-OVA system showed comparable stability (**Fig. S14b**). The radiolabeling stability analysis confirmed that the nanoparticles were stable when challenged, and therefore suitable for *in vivo* tracking of both nanovaccine components.

Consistent with the MRI studies, SPECT/CT images and *ex vivo* analysis of mice injected with ^{67}Ga-labelled mZnSPION-polyIC-R837 (**Fig. 7d-g**) showed that the particles remain mostly at

in different organs revealed that 24 h post-injection, some migration had occurred to the tumour and to the inguinal and axillary LNs (0.02-0.375 % of the injected dose, **Fig. 7g**).

Notably, ^{67}Ga-labelled mSPION-OVA system migrated faster showing clear accumulation in draining LNs and in LNs distant from the injection site already 3 h post-injection. mSPION-OVA was also detected in the tumour at 24 h and 48 h (**Fig. 8**). Moreover, even when the ^{67}Ga-labelled mSPION-OVA was injected into the left hind hock of mice, the accumulation of ^{67}Ga-labelled mSPION-OVA in LNs and tumour is higher than for peritumourally injected ^{67}Ga-labelled mZnSPION-polyIC-R837 (**Fig. S15** and **Fig. 7**). A similar migration pattern was found in tumour-free mice (**Fig. S16**).

Overall, combination of MRI and SPECT/CT imaging reveals differences in the migration capacity of the nanovaccine components. In the case of mSPION-OVA a higher proportion of nanoparticles can enter directly the lymph to provide higher accumulation in LNs and tumour within the first hours of administration, whereas the mZnSPION-polyIC-R837 system is effective at creating a depot at the site of injection from which the adjuvant nanoparticles can migrate more slowly to draining LNs and tumour. In this way we propose that the nanoparticles allow antigen to be processed quickly to initiate T-cell priming events within the first hours of administration and are able to sustain the responses over longer periods. The slow release of pro-inflammatory stimuli by mZnSPION-polyIC-R837 provides a way to enhance endocytic antigen uptake by DCs in the skin, initially leading to loss of DC motility as shown by the downregulation of CCR7 (**Fig. 2e**). This can be followed by a characteristic maturation period whereby the slow moving wave of DCs regain their mobility and undergo a switch of

eventually migrating to LNs to induce full-fledged effector responses.[50]

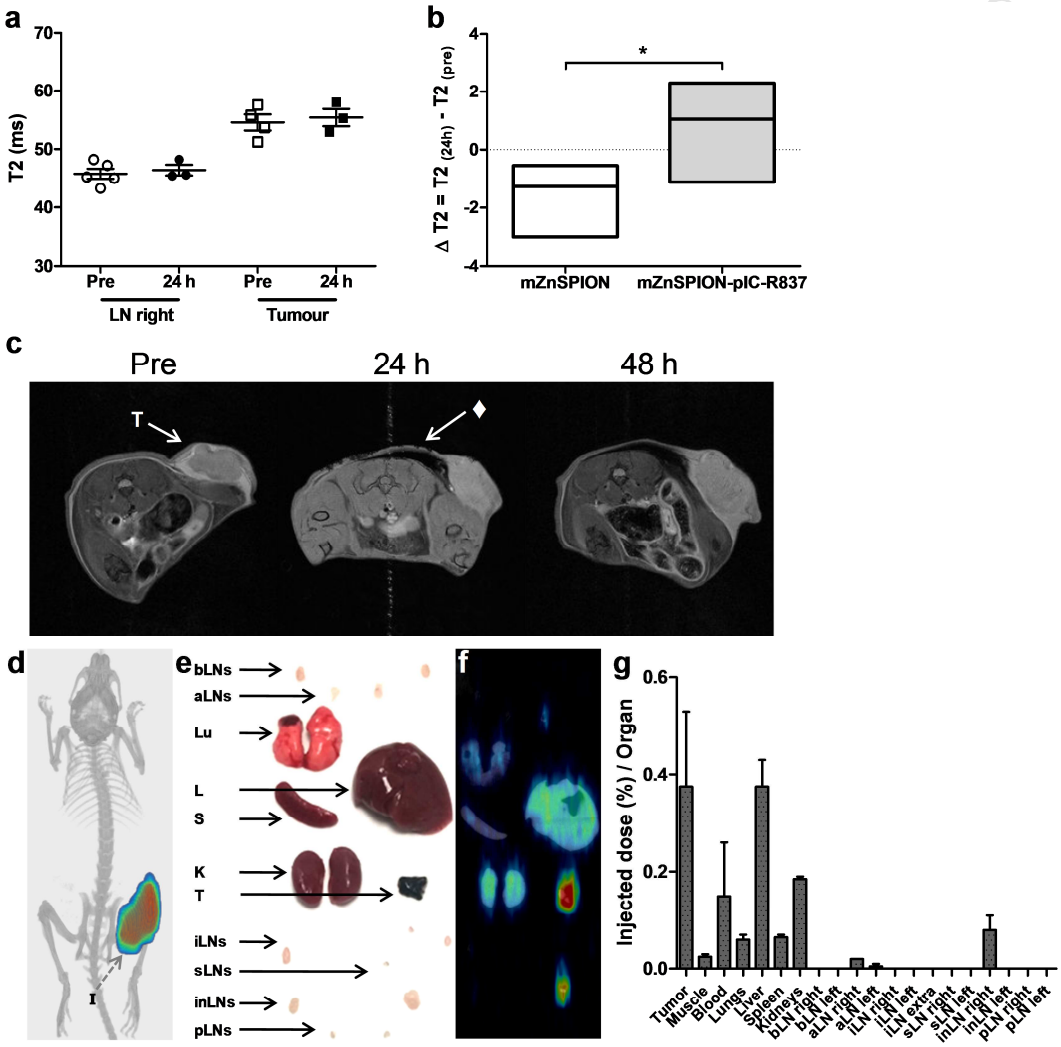

Fig. 7. *In vivo* tracking of mZnSPION(-polyIC-R837). T_2-weighted MR imaging at 7T (a-c). (a) Quantitative analysis of T_2-weighted images in the right inguinal lymph node and tumour before and 24 h after s.c. injection of mZnSPION-polyIC-R837 into the peritumoural region (100 mL, [Fe] = 6 mM). (b) Differences in T_2 in the inguinal lymph node of mice administered mZnSPION or mZnSPION-polyIC-R837. (c) T_2-weighted images of B16-F10(OVA) tumour bearing mice before and at different time points after s.c. injection of mZnSPION-polyIC-R837 (T, tumour; ♦, injected sample). SPECT/CT images and *ex vivo* analysis of mice injected with ^{67}Ga labelled mZnSPION-polyIC-R837. Tumour bearing mice were injected with radiolabelled micelles into

selected harvested organs, (f) SPECT/CT image of the harvested organs and (g) biodistribution expressed as percent injected dose per organ. I, injected sample; T, tumour; bLN, brachial LN; aLN, axillary LN; Lu, lungs; L, liver; S, spleen; K, kidneys; iLN, iliac LN; sLN, sciatic LN; inLN, inguinal LN; pLN, popliteal LN. Data presented as mean ± SEM. n = 2-5 mice per group. *P<0.05 by t test (unpaired).

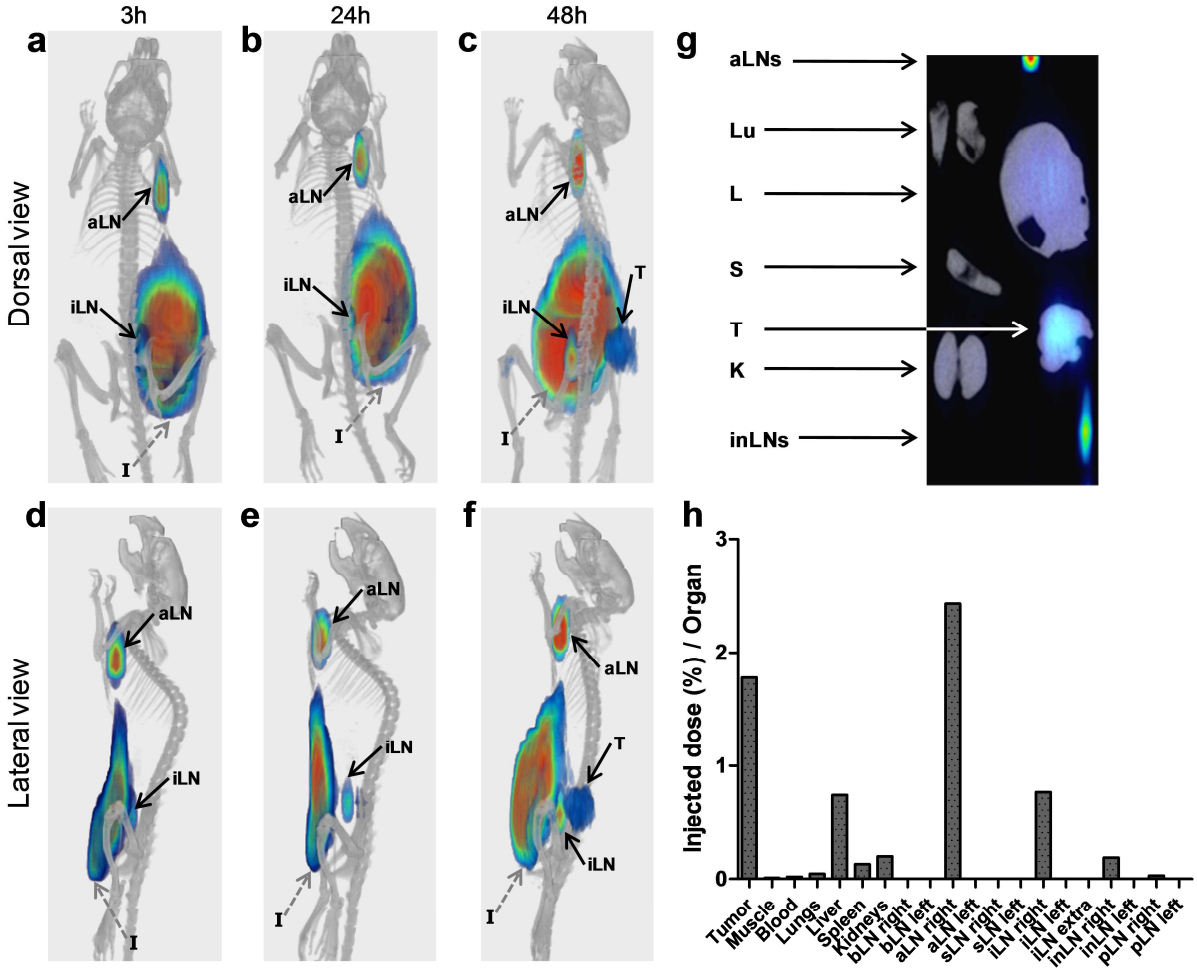

Fig. 8. SPECT/CT images of melanoma tumour bearing mice after s.c. injection of ^{67}Ga labelled mSPION-OVA (20.7 µg of SPION, 41.0 MBq) into the flank. (a, d) 3 h, (b, e) 24 h and (c, f) 48 h post-injection. (a-c) dorsal and (d-f) lateral views of *in vivo* images at different time points are shown. (g, h) SPECT/CT image of the harvested organs and biodistribution expressed as percent injected dose per organ. I, injected sample; T, tumour; bLN, brachial LN; aLN, axillary LN; Lu, lungs; L, liver; S, spleen; K, kidneys; iLN, iliac LN; sLN, sciatic LN; inLN, inguinal LN; pLN, popliteal LN.

Discussion

TLR agonists, by activating a broad range of innate immune cells and directly killing different types of cancer cells including melanoma cells, offer unique mechanisms of maximizing anti-tumour immunity. However, high doses are often required to elicit a strong enough response, leading to unacceptable toxicity. Studies have shown that scientifically rational combinations of TLR agonists can synergistically activate immune responses,[38,39,81] offering the potential to achieve strong antitumour immune responses using much lower doses. There is growing evidence that in targeted delivery of TLR agonists and tumour antigen both nano and microparticle-based systems can provide enhanced antitumour immunity compared to the free drugs.[8,16,51,82,83] This suggests that optimizing the anti-cancer efficacy of TLR-targeted therapeutics may require using delivery systems that promote and combine different ways of interaction with antigen presenting cells at both the site of injection and target tissue, exploiting the dynamic nature of nanoparticles *in vivo* (e.g. initial size, biofunctionalisation, aggregation, etc.). However, this aspect has not been investigated so far. Our data demonstrate that the combination of polyIC and imiquimod synergizes to create a potent adjuvant for the development of effective antitumour vaccines, eliciting robust T-cell and antibody responses to tumour antigen at low doses and avoiding systemic adjuvant toxicity and morbidity. We have shown that the antitumour immune responses generated with this combination of TLR agonists co-administered with tumour antigen can be significantly enhanced by targeted delivery using micelles filled with 5 nm MNPs, which help to regulate the trafficking and processing of antigen and adjuvant by antigen presenting cells, and by PD-L1/PD-1 immune checkpoint inhibition. We optimized the magnetic properties of the MNPs by controlled zinc(II) doping, and carried out organic chemistry-free radiolabeling with ^{67}Ga for enhancing *in vivo* multimodal imaging (MRI

subcutaneous site of injection to draining LNs and tumour due to differences in size and biofunctionalisation.

TLR agonists have been extensively investigated for vaccine formulations with promising results. However, they have been used mainly acting singly and as a monotherapy, limiting their efficacy and giving rise to systemic toxicity. Among these drugs those targeting endosomally localized TLR3, TLR9 and TLR7/8 are ideal candidates for benefiting from nanoparticle delivery. Herein, we investigated the effect of co-activation of TLR3 and TLR7 using polyIC and imiquimod, respectively; two drugs with demonstrated antitumour efficacy when used as single drugs and with considerable potential to complement and/or synergize in their antitumour functions due to their known mechanisms of action. Thus, all TLRs signal through the myeloid differentiation primary response protein 88 (MyD88)-dependent pathway, except TLR3 that primarily uses the toll/interleukin-1 receptor domain-containing adapter-inducing interferon-β (TRIF)-dependent pathway.[84] Moreover, polyIC is not only a TLR3 ligand but also a MDA5 agonist.[85] This makes polyIC of great interest as a potential anti-cancer agent. TLR3 and MDA5 are expressed both by immune cells and by cancer cells and studies have demonstrated distinct yet complementary roles for MDA5 and TLR3 in polyIC-mediated activation of DCs and NK cells and pro-apoptotic activity against tumour cells, leading to profound antitumoural effects in different tumours. The main antitumoural activity of imiquimod is driven by TLR7-mediated induction of pro-inflammatory cytokines, chemokines and other mediators by DCs to induce a profound T-helper (Th1)-weighted antitumoural cellular immune response.[62] However, several studies have shown that imiquimod enhances also antigen-specific activation

exerts Bcl-2- and caspase-dependent pro-apoptotic activity against some tumour cells. [95–97]

Our data confirm that combinations of polyIC and R837 provide synergistic activation of macrophages and dendritic cells, which show different sensitivity to each individually and when combined, and that R837 could directly kill the target melanoma cells. Indeed, this has made imiquimod useful for melanoma treatment,[98,99] while other studies showed that not every cancer cell line can be killed by polyIC.[67] However, the polyIC-R837 complexes in small doses enabled generation of strong immune activation at lymphoid tissue without inducing potentially toxic systemic cytokine release. We evaluated the effectiveness of vaccination with and without nanoparticle vehicles on the induction of antitumour immunity in an aggressive and poorly immunogenic mouse melanoma model using B16-F10 melanoma cells expressing OVA and the immune inhibitory transmembrane protein PD-L1. It has been shown that an optimal anti-cancer treatment regime for the TLR7 agonist R848 (resiquimod) requires the possibility for sustained stimulation, which was achieved using cycles of repeated R848 injection.[100] Here, instead we used the slow migration of the mZnSPION-polyIC-R837 system from the s.c. injection site to LNs and tumour to achieve the sustained activation of APCs. On the other hand, it is known that a low antigen dose is required to generate the high-avidity T-cells that provide more potent responses against tumours and pathogens, but it has been proven difficult to induce these T-cells through vaccination.[101,102] Several authors have reported efficacy of anti-tumour prophylactic and/or therapeutic vaccines with reduced antigen doses in the range of 10-100 µg/mouse.[12,103–109] Here, we demonstrate the combined effect of using polyIC-R837 as potent adjuvant and mSPION for OVA delivery. Mice immunized with 5 µg of OVA and polyIC-R837 delivered by the MNP-filled micelles developed long term protection against the

days after the last immunization, which is consistent with a strong memory effect.

Another paradigm in immunology is that kinetics of antigen and DC migration are key parameters with regard to T-cell and anti-tumour responses, adaptive immunity and tolerance.[48,110] The data presented here extend recent findings on nanoparticle delivery of TLR agonists to an effective combination of TLR agonists. In the context of TLR agonist and antigen delivery, it may be important to consider the different migration and dynamic aggregation of the nanoparticles *in vivo*. Currently it is not known which type of particles are preferred for generating the most effective antitumour immunity, namely, those that are small and passively traffic to LNs or those that by being larger can exploit uptake by DCs in the periphery to reach the LNs, or whether the best results are obtained by specific combinations of the two. The mZnSPION-polyIC-R837 system displayed more tendency to aggregate, and by combination of MRI and SPECT/CT imaging we showed that are retained longer at the site of injection with a small percentage of particles reaching the draining LNs. On the other hand, the mSPION-OVA system aggregated less, migrated faster from the injection site and provided higher accumulation in the LNs at least until 48 h post-injection.

Although checkpoint inhibitors are an important breakthrough, this therapy does not show any clinical benefit in most patients (70%-80%), and thus now the focus is on combination immunotherapy approaches [111],[112] It has been recently shown that combined administration of poly-IC and anti-PD-L1 mAb into tumour-bearing mice is able to generate potent immune responses resulting in the complete eradication or remarkable reduction of tumour growth.[113] The study suggested that this type of combination immunotherapy treatment would work even in cases where no reliable tumour associated antigens capable of eliciting effective antitumour T-

C57BL/6 is very inefficacious and it only works in combination therapies.[114] We explored the potential of a combination treatment bringing immunization with OVA + polyIC-R837 together with the B16-F10(OVA) melanoma cell with silenced PD-L1. PD-L1 blockade achieves the same effects than knocking out PD-L1 in cancer cells as demonstrated previously.[78] However, while administration of blocking antibodies may have uncontrolled systemic effects, here we focused on the specific effects over cancer cells without affecting other factors such as antigen presentation in peripheral tissue. Directly evaluating the relative roles of PD-L1 expression by the tumour and host cells in the suppression of anti-tumour immune responses is emerging as a central and controversial unknown to be able to understand and predict the therapeutic benefit from antibodies interfering with PD-L1 activity.[115] Although it should be of no surprise that we observed enhanced protection against the tumour challenge with 100 % rate of response to the treatment, even for the nanoparticle-free vaccines, it is an important result. It provides support for the combinatorial immunotherapy approach using the checkpoint inhibitors and potentially quick clinical translation. Hence, the immunotherapy treatment described here uses drugs that are already used clinically or are currently undergoing clinical testing.

Many nanosystems used for application in cancer are difficult to synthesize. The preparation of mZnSPION-polyIC-R837 is fully by self-assembly, mimicking the formation of liposomal formulations. This provides a further framework for future clinical translation. Moreover, while the present work shows effective long term protection against a syngeneic aggressive melanoma challenge with a simple system, this system offers the possibility for tackling control of established tumours by multi-pronged strategies that exploit further the magnetic properties of the delivery vehicles (e.g. hyperthermia, magnetically guided drug delivery), and/or are

delay tumour growth and synergize with anti-cancer vaccines.

Acknowledgements. This work was supported by the Spanish Ministry of Economy and Competitiveness (MINECO) grants CTQ2011-22723 and CTQ2014-54761-R and FPI graduate studentships to A. I. B. G. and M. J. G. G. A. R. de A. acknowledges a PhD studentship from the Department of Education, Language Policy and Culture of the Basque Government. We thank Luis Yate for XPS studies and Dr. Pablo Sarobe (CIMA, University of Navarra) for the B16-F10(OVA) cells.

Materials and methods

Synthesis and characterization of SPION and ZnSPION. The hydrophobic magnetic nanoparticles, (SPION and ZnSPION ($(Zn_xFe_{1-x})Fe_2O_4$; $x \leq 0.5$)) were prepared adopting previously described precedures.[116,117] The size of the MNPs was determined by transmission electron microscopy (TEM) on a JEOL JEM-2011 electron microscope operating at 200kV. The samples were prepared by depositing a drop of MNPs onto a copper specimen grid coated with a holey carbon film (*Electron Microscopy Sciences*). Samples were prepared by dissolving 1 mg of nanoparticles in THF to a final concentration of 0.1 mg/mL. At least 300 particles were measured using the Image J software to determine MNP size. The Fe and Zn concentration in the samples was determined by ICP-OES analysis carried out by the SGIker analytical facility of the University of the Basque Country (UPV/EHU; Leioa, Spain). ICP-OES was carried out using a Perkin Elmer Optima 5300 DV, employing an RF forward power of 1400 W, with argon gas flows of 15, 0.2 and 0.75 L/min for plasma, auxiliary and nebulizer flows, respectively. Using a peristaltic pump, sample solutions were taken up into a Gen Tip cross-Flow

axial mode. The selected wavelengths (238.024, 239.562, 259.939 nm) were analyzed in fully quant mode (three points per unit wavelength). A range of calibration standards were prepared using single element 1000 mg/L stock solutions (*Fisher Scientific UK LTD*) and a Merck multi element standard (ICP Multi element standard solution VI CertiPUR®, *Merk*) was employed as a reference standard. XPS experiments were performed in a SPECS Sage HR 100 spectrometer with a non-monochromatic X-ray source (aluminum Kα line of 1486.6 eV energy and 350 W). The samples were placed perpendicular to the analyzer axis and calibrated using the $3d_{5/2}$ line of Ag with a full width at half maximum (FWHM) of 1.1 eV. The selected resolution for the spectra was 10 eV of Pass Energy and 0.15 eV/step. Measurements were made in an ultra high vacuum (UHV) chamber at a pressure below $8 \cdot 10^{-8}$ mbar. Magnetic measurements were carried out in a 7T SQUID magnetometer at the Magnetic Measurements Service of the University of the Basque Country (UPV/EHU; Leioa, Spain).

Synthesis and characterization of mZnSPION(-polyIC-R837) and mSPION(-OVA). mSPION, mSPION-OVA and rhodamine-labelled micelles were prepared as described previously.[58,70,118] For the synthesis of mZnSPION, different ZnSPION-to-lipid ratios were used to optimize the micelling process and the properties (e.g. size). The reported results were obtained with micelles prepared with a oleic acid-coated ZnSPION:DPPE-mPEG(2000) weight ratio of 1:5. The micelle size and zeta potential analysis was measured with a NanoSizer (*Malvern Nano-Zs*, UK). For size measurements samples were diluted in water, and for zeta-potential measurements in nanopure water with NaCl 0.09 %. The results are a mean of at least three measurements matching quality criteria. Relaxivity measurements were carried out at 37 ^{0}C on a Bruker Minispec mq60 instrument operating at 1.47 T. T_1 and T_2 values were measured for

respectively. The relaxivity values, r_1 and r_2, were calculated through linear least squares fitting of 1/relaxation time (s^{-1}) *versus* the iron concentration ([Fe] mM). The MRI phantom experiments were carried out on a Bruker Biospec 7 T with a 12 cm gradient capable of delivering 400 mT/m using a 40 mm volume coil. T_2-weighted images were acquired by using Bruker's MSME (Multi slice Spin echo) sequence. The echo time (TE) values were varied in 128 steps ranging from 10 ms to 1280 ms and a repetition time (TR) of 15 s. T_1 maps were obtained by using a spin echo sequence. Images were acquired at ten different TR values 150, 500, 1000, 1500, 2200, 3000, 4000, 5200, 7.600, 17500 ms). All data were acquired with: 256 x 256 points and a Field of View of 3 cm x 3 cm, slice thickness of 1.5 mm, no gap between slices and one average. The T_1 and T_2 map images were calculated using the Bruker's Paravision 5.1 software via the Levenberg-Margardt method.

For biofunctionalisation with the TLR agonists, lyophilized polyIC and imiquimod (*Invivogen*) were resuspended in endotoxin-free water to a final concentration of 1000 µg/mL and 500 µg/mL, respectively. Double-functionalized MNPs were prepared through a two-step process. The mZnSPION solution (500 nM of nanoparticle) was mixed with the poly(I:C) solution (156 µg/mL) and the mixture was stirred overnight at 700 rpm at room temperature. The unbound poly(I:C) were removed with three cycles (1500 × g, 5 min) of ultrafiltration with NanoSep 100k (MWCO 100 kDa) centrifugal devices (*Pall Life Sciences*).Then, the formed mZnSPION-polyIC micelles were resuspended in imiquimod solution (250 µg/mL), keeping the final volume constant. These mixtures were stirred and purified as described for the polyIC adjuvant. The final pellet was resuspended in the same initial volume of nanopure water or 10 mM PBS and stored at 4 °C. The quantification of bound imiquimod was performed by UV-visible spectroscopy

imiquimod. Once the amount of R837 was estimated solutions containing free polyIC + R837 (polyIC titrated into the solution of R837) were analyzed by UV-vis and compared against mZnSPION-polyIC-R837 – mZnSPION at the same iron concentration determined by ICP-OES to ensure that vaccines and nanovaccines had the same amount of polyIC-R837. Release experiments were carried out incubating the mZnSPION-pIC-R837 sample in 10 mM PBS under continuous stirring. Released drugs were analyzed by UV absorption spectroscopy after ultrafiltration with NanoSep 100k (MWCO 100 kDa) centrifugal devices. UV absorption spectra were acquired using a NanoDrop ND 1000 (version 3.5.2) Spectrophotometer (*NanoDrop Technologies*). Fluorescence experiments to assess the interaction of imiquimod with polyIC were conducted in a Fluoromiter Fluorolog-TSPC (*Horiba-Jovine Ivone*) by irradiating the samples with an excitation wavelength of 250 nm. TEM images, ICP-OES analysis and DLS measurements of the (biofunctionalised) samples were acquired as described above for the "naked" MNP-filled micelles.

Localization of intracellular micelles by confocal microscopy and flow cytometry. The J774.A1 murine macrophage cell line was purchased from the ATCC and cultured in DMEM supplemented with 10 % FBS, 1 % L-glutamine (all from *Gibco, Life Technologies*) and 1 % penicillin-streptomycin (P/S; *Sigma Aldrich*), and maintained in a humid atmosphere at 37 °C and 5 % CO_2. For confocal microscopy imaging, the J744.A1 cells were seeded in poly-lysine-coated 35 mm glass bottom dishes (*MatTek*) in 2 mL of complete DMEM medium. Then, cells were incubated for 1 h at 37 ºC and 5 % CO_2 in media containing rhodamine-labelled mZnSPION-polyIC-R837 (25 nM of nanoparticle), 1 µM LysoTracker Green DND-26 (*Invitrogen*) and 3 drops of NucRed® Live 647 ReadyProbes® Reagent (*Life Technologies*). All

magnification oil lens. Fluorescence images were taken in sequential mode at the excitation wavelengths of 488 nm, 561 nm and 633 nm for LysoTracker Green DND-26, rhodamine B or NucRed® Live 647 ReadyProbes® Reagent, respectively. The thickness of each optical slice was set at 3 µm for each color channel. Transmitted light images were also acquired. Image analysis was performed using the software Zeiss LSM Image Browser. In the case of uptake studies by flow cytometry, J774.A1 cells were plated in 96-well plates (1×10^5 cells/well) and allowed to adhere overnight in DMEM medium supplemented as described before. Fluorescent MNPs were diluted in medium and added to cells, which were maintained at 37 °C, 5% CO2 during 1 h, 3 h or 24 h. Then, the medium was removed and cells were transferred to cytometer tubes by gentle pipetting in sterile PBS and pellet down by centrifugation (580 x g, 5 min, 4 °C). Cells were resuspended in a final volume of 200 µL of FACS buffer (1% BSA in 10 mM PBS). Rhodamine uptake was measured using a FACS Canto II flow cytometer (*BD bioscience*) and the data were analysed using the FlowJo, LCC software. J774A.1 cells were electronically gated based on the forward and side scatter parameters and the not-single events left out based on forward area and height scatter parameters. Rhodamine signal coming from the MNPs-filled micelles was analysed within this population.

Cytotoxicity and cytokine production studies. To assess cytokine production at 24 h, J774.A1 cells were seeded at 2.5×10^4 cells/well (100 µL per well) in flat bottom 96-well plates and allowed to adhere overnight. Then, medium was removed and cells were left untreated or treated with the immunostimulatory formulations and the corresponding controls, diluted accordingly in medium, in triplicate. After 24 h, cell supernatant was removed and frozen for subsequent cytokine analysis and cytotoxicity assay (*vide infra*). The B16-F10(OVA) murine skin melanoma

gifted by the group of Dr. Pablo Sarobe (Center of Applied Medical Research, CIMA, Pamplona, Spain). These cells were cultured in RPMI-1640 (*Lonza*) supplemented with 10 % FBS, 1 % L-glutamine and 1 % P/S, and maintained in a humid atmosphere at 37 °C and 5 % CO_2. To assess cell viability at 24 h, 48 h and 72 h, cells were seeded at 7×10^3, 2.5×10^3 and 1.5×10^3 cells/well (100 µL/well), respectively, in flat bottom 96-well plates and allowed to adhere overnight. Media was removed from each well prior to adding 100 µL of each sample, properly diluted in cell culture media, per well and in triplicate. To determine cell viability, 100 µL/well of MTT reagent (*Roche*) diluted in media to a final concentration of 0.25 mg/mL was added after removal of the supernatant. After 1 h incubation at 37 °C, the reagent was removed and 200 µL/well of DMSO were added to solubilize formazan crystals. Finally the optical density of the samples was measured in a TECAN Genios Pro 96/384 microplate reader at 550 nm and data was represented as the percentage of cell survival compared to control wells.

BMDC maturation assay. BMDCs were prepared as described previously.[70] The various immunostimulatory formulations (100 µL per well, appropriately diluted in complete RPMI-1640) were added to the DC containing wells (2×10^5 cells per well in 96-well plates) and incubated for 24 h in a humid atmosphere at 37 °C and 5 % CO_2, following which supernatants were recovered and frozen for later testing of cytokines. For maturation markers expression, after 24 h incubation with the various formulations, BMDCs were washed with PBS, incubated with anti-CD16/CD32 (*BD Biosciences*), and then stained with fluorophore-labelled antibodies against CD11c, MHC-II, CD80, CD86 and CCR7 (*Biolegend*), following the manufacturer's instructions. Finally, cells were washed with FACS buffer, resuspended in 200 µL of FACS buffer and analyzed by flow cytometry. The DC population was defined as $CD11c^+$ $MHC\text{-}II^+$,

were included in each assay.

Quantification of cytokines and antibody production by ELISA. IL-6 and IL-12 were measured in cell supernatants using sandwich ELISA following the manufacturer's instructions (murine IL-6 mini EDK ELISA kit, *R&D Systems*; murine IL-12 mini EDK ELISA kits, *Peprotech*). A 4-parameter sigmoidal (logistic) standard curve was used to quantify cytokines (GraphPad Prism 5 software). Results are expressed as mean ± SEM in pg/mL or ng/mL. Anti-OVA IgG1, IgG2c and IgGt antibodies were measured in blood serum using indirect ELISA. Flat bottom 96 well EIA/RIA plates (*Corning*) were covered with 50 µL/well of OVA diluted in PBS to a final concentration of 0.04 mg/mL. The samples of blood serum were obtained from immunized mice by facial vein puncture and centrifuged at 13000 × g for 5 min to remove the cellular content of the blood. The concentrations of antigen-specific antibodies were determined with HRP-conjugated anti-mouse IgG1, IgG2c and IgGt antibodies (*BioRad*) diluted 1:4000, 1:10000 and 1:500 in PBS, respectively. The results were expressed as the $\log_{10}$ value of the reciprocal of the endpoint dilution which gave an optical density (O.D.) of 0.2 or above, after the subtraction of the background levels. In both ELISA types, the measurement of each sample was conducted in duplicate. Absorbance measurements were carried out in a TECAN Genios Pro 96/384 microplate reader at 450-550 nm.

***In vivo* immunization and cancer immunotherapy studies.** Animals were cared for and handled in compliance with the Guidelines for Accommodation and Care of Animals (European Convention for the Protection of Vertebrate Animals Used for Experimental and Other Scientific Purposes) and internal guidelines, and all the experimental procedures were approved by the

diet *ad libitum*.

For the analysis of innate immune responses, C57BL/6J female mice (6-8 weeks old) were vaccinated with the various formulations diluted in PBS by injection (40 µL/mouse) into the hock (3 µg polyIC/mouse, 1 µg imiquimod/mouse and 4.8 µg ZnSPION/mouse). After 24 h, the spleen and inguinal and popliteal LNs were harvested and processed as described previously[70] for further analysis of the maturation of DC and NK cellular populations. Briefly, 1×10^6 cells/well diluted in RPMI-1640 were seeded in a 96-well plate and divided into two different staining panels. For the DC maturation analysis, cells were stained as described in the *in vitro* BMDC maturation assays, analyzing this time an additional maturation marker, CD40 (*Biolegend*). NKs cells were stained with CD3, NKp46 and CD69 antibodies, and the corresponding isotype control (*Biolegend*). The NK population was defined as $CD3^-$ $Nkp46^+$, and CD69 expression was analyzed into this gated population.

For assessing adaptive immune responses *in vivo*, C57BL/6J mice (6-8 weeks old) were immunized on day 0 (prime) and 14 (boost) with the different formulations injected s.c. into both flanks (100 µL/flank). Blood extraction was carried out by facial vein puncture at the indicated time points pre- and post- injection. Immunizations assessed in independent experiments with 5 µg OVA/mouse and adjuvant doses ranging from 3-4 µg poly(I:C)/mouse, 0.5-1.3 µg imiquimod/mouse administered alone or with micellar delivery vehicles at 6-10 µg/mouse ZnSPION and 45-55 µg/mouse SPION produced similar results. Three weeks after the last immunization, mice were analyzed for the percentages of SIINFEKL-specific $CD8^+$ T-cells in blood, spleen and inguinal LNs, by staining with CD8 and CD3 antibodies (*Biolegend*) to define

the OVA specific T-cell percentage in each organ of interest.

For prophylactic tumour challenge studies, vaccinated C57BL/6J female mice (6-8 weeks old) were challenged one week after the last immunization by s.c. injection of 3×10^5 B16-F10(OVA) tumour cells. Mycoplasma test (*Lonza*) was carried out prior to injection to ensure that cells were free of contamination. Tumours were measured every two to three days with a digital caliper and volumes (V) were calculated as V (mm^3) = [(short diameter)^2 x (long diameter)]/2. Mice were considered tumour-free until dermal lesions were visible or palpable. For survival rate evaluation, mice were kept until sacrifice was necessary once the tumour reached a diameter of ≥ 15 mm or when tumour necrosis or ulceration signs appeared. 63 days after the first tumour challenge, healthy mice were s.c. re-challenged with 3×10^5 B16-F10(OVA) cells. Immunizations with OVA + polyIC-R837 and mZnSPION-polyIC-R837 were carried out in independent experiments three times.

Effector memory and central memory $CD8^+$ T cell populations were defined as $CD44^+CD62L^+$ and $CD44^+CD62L^-$, respectively, inside the $CD3^+$ and $CD8^+$ double positive population. OVA specific T-cell percentage in this population was analyzed as previously described. To study intracellular IFN-γ and TNF-α and the expression of the degranulation marker, 1×10^6 cells/well were placed in a 96-well plate in 100 µL of RPMI-1640 medium in the presence of BD Golgi Stop, the anti-CD107a antibody (LAMP-1 protein) and 10 µg/mL SIINFEKL in RPMI-1640 medium. After 5 h of incubation at 37 °C, cells were washed twice and stained with the surface markers (CD3 and CD8). Then, cells were fixed and permeabilised (BD Cytofix/Cytoperm fixation and permeabilisation kit), after which intracellular cytokine staining was performed (anti-INF-γ and -TNF-α antibodies). T cells were gated based on double positive for CD3 and

cell percentage of total $CD3^+$ $CD8^+$ T cells. Isotype controls were included in intracellular cytokine analysis by flow cytometry assay and were not included in the figures for clarity purposes. Results were expressed as mean ± SEM of 5 mice per group of immunization, analysed individually and compared to unstimulated wells.

For creating the B16-F10(OVA) with knock-down expression of PD-L1 (B16-F10(OVA) ΔPD-L1), lentiviral particles for silencing the expression of PD-L1 were produced in 293T as described previously.[78] Cell culture supernatants were harvested, filtered through 0.45 µm filter and ultracentrifuged for lentivector purification. Lentiviral particles were titrated and used to transduce B16-F10(OVA) cells. Knockdown cells were selected by antibiotic pressure with increasing concentrations of puromycin. Similarly to the prophylactic immunization assays described above, C57BL/6J female mice (6-8 weeks old) were challenged one week after the last immunization by s.c. injection of 3×10^5 B16-F10(OVA) ΔPD-L1 cells. In this case, however, due to the slower tumour growth the re-challenge was carried out with 1.5×10^6 B16-F10(OVA) ΔPD-L1 cells/mouse 35 days after the first challenge.

Imaging studies. Tumours were left to settle and grow until the diameter reached around 7 - 12 mm before imaging acquisition.

For MR *in vivo* experiments, at the beginning of the experiments, mice were immunized with mZnSPION-pIC-R837 at a concentration of 6 mM Fe. 100 µL of sample were s.c. injected in the tumour vicinity. Images were acquired at times prior injection, 24 h and 48 h post-injection to analyze accumulation of nanoparticles. Animals were anesthetized prior to imaging using 3.5 % isofluorane and maintained at 1.5 – 2.5 % isoflurane in 100 % O2 and at a constant body

Bruker Biospec system (*Bruker Biospin GmbH*, Ettlingen, Germany) using the BGA12-S mini imaging gradient and 40 mm inner diameter transmit/receive mouse body volumetric coil. Axial gradient echo experiments were performed with the following parameters: A respiration synchronized (TR = one respiration cycle) FLASH sequence, TE = 3 ms, FOV = 28 mm x 28 mm, Matrix = 256 x 256, Slice Thickness = 0.75 mm, N Slices= 32 and 2 averages. Axial T_2-weighted images were acquired using the following parameters: A respiration synchronized (TR = 4 respiration cycles) Multi Slice Multi Echo (MSME) sequence, TE = 8, 16, 24, 32, 40, 48, 56, 64 ms; FOV = 28 mm x 28 mm, Matrix = 128 x 128, Slice Thickness = 0.75 mm, N Slices= 9 and 2 averages. The images were fitted into Levenberg-Margardt method to calculate T_2 values using Bruker's Paravision 5.1 software.

To carry out *in* vivo SPECT/CT studies, MNPs were labelled with Gallium-67. Radiolabelling was carried out using a ^{67}Ga citrate solution purchased from Molypharma (Spain) (specific activity =1.4 TBq/μmol), which was first converted into $^{67}GaCl_3$. Briefly, the ^{67}Ga citrate solution was passed through a light silica column cartridge (Sep-Pak, *Waters*) to selectively retain the radiometal. The cartridge was washed with ultrapure water (10 mL) and ^{67}Ga was finally eluted with HCl 0.1 M solution. The eluate was collected in different 100 μL fractions, and only those containing the maximum activity concentration were used in subsequent labeling experiments. The eluted ^{67}Ga chloride solution (100 μL, c.a. 110 MBq) was then mixed with 100 μL of mZnSPION-pIC-R837 or mSPION-OVA micelles solution and diluted up to final volume of 400 μL in acetate buffer (pH = 3.8 ± 0.1). After incubation at 70 °C during 30 min, the reaction crude was cooled down to room temperature, the labelled MNPs were separated via centrifugal filtration (3354 x g for 10 min) using AmiconUltracel 100k (MWCO 100 kDa)

from the filter by the addition of PBS (100 μL). The total radioactivity in the filtrates and retentates was measured in a CRC-25R dose calibrator (*Capintec*, USA) in order to determine the incorporation efficiency. For stability studies, one batch of ^{67}Ga-mZnSPION-pIC-R837 or mSPION-OVA was fractioned in different aliquots, which were incubated in the presence of DOTA chelating agent (c.a. 10^6 moles of DOTA per mole of nanoparticle) at 37 °C. At different time points, the samples were filtered in order to separate the NPs from the ^{67}Ga complexed to DOTA, and radioactivity in the retentate and in the filtrate was measured with the CRC-25R dose calibrator. The dissociation of ^{67}Ga (expressed in percentage) from the radiolabelled micelles at each time point was calculated as the ratio between the amount of radioactivity in the filter and the starting amount of radioactivity. For *in vivo* imaging studies, tumour bearing mice were immunized with ^{67}Ga-labelled mZnSPION-pIR-R837 or mSPION-OVA dissolved in PBS to a concentration of 1.2 or 6 mM Fe, respectively. 50 μL of sample/mouse were s.c. injected in the tumour vicinity, in the ventral flank or in the hind hock. Animals were anesthetized prior to imaging using 3.5 % isofluorane and maintained at 1.5 – 2.5 % isoflurane in 100 % O_2 during the whole acquisition. Whole-body SPECT/CT scans were acquired at 3 h, 24 h and 48 h post-injection using the eXplore speCZT CT preclinical imaging system (*GE Healthcare*, USA). With the full ring detector, 360° of data were acquired by rotating the collimator 45° (45 steps, 1°/step). Data were collected in an energy acquisition window from 125−150 keV to 84−102 keV and acquisition times from 60 min (80 s/step) to 45 min (60 s/step). An 8-slit collimator was used with a field of view of 32 and 78 mm in the transaxial and axial directions, respectively. After each SPECT scan, CT acquisitions were performed to provide anatomical information on each animal. The CT acquisition consisted of 220 views in 0.88° increments around the animal

images were reconstructed using the OSEM iterative algorithm (5 and 15 subsets, 3 and 5 iterations) into 128 × 128 × 32 array with a voxel size of 0.4 × 0.4 × 2.46 mm, and were not corrected for scatter and attenuation. The CT images were reconstructed using a cone beam filtered back-projection Feldkamp algorithm into 437 × 437 × 523 array with a voxel size of 0.2 × 0.2 × 0.2 mm. At the end of the scanning procedure, the mice were culled by cervical dislocation and organs of interest removed. Analysis of the injected dose percentage per organ was performed by measuring their activity with a WIZARD22470 Automatic Gamma Counter (*PerkinElmer*).

Statistical analysis. Data presented as mean ± SEM. The differences between the control and the experimental groups were assessed using two-tailed unpaired Student's t tests and the differences among groups > 2 by one-way or two-way ANOVA (GraphPad Prism, GraphPad Software, La Jolla, CA). P values of less than 0.05 were considered statistically significant.

Competing financial interests. The authors declare no competing financial interests

Appendix A. Supplementary data

Data availability statement

The raw/processed data required to reproduce these findings cannot be shared at this time due to technical or time limitations

5. References

[1] A.Z. Wang, R. Langer, O.C. Farokhzad, Nanoparticle Delivery of Cancer Drugs, Annu. Rev. Med. 63 (2012) 185–198. doi:10.1146/annurev-med-040210-162544.

[2] P. Couvreur, Nanoparticles in drug delivery: Past, present and future, Adv. Drug Deliv. Rev. 65 (2013) 21–23. doi:10.1016/j.addr.2012.04.010.

[3] T.L. Doane, C. Burda, The unique role of nanoparticles in nanomedicine: imaging, drug

(2013) 9518–9525. doi:10.1021/nn405674m.

[5] J. Shi, P.W. Kantoff, R. Wooster, O.C. Farokhzad, Cancer nanomedicine: progress, challenges and opportunities., Nat. Rev. Cancer. 17 (2017) 20–37. doi:10.1038/nrc.2016.108.

[6] T. Lammers, Cancer nanomedicine: is targeting our target?, Nat. Rev. Mater. 1 (2016). doi:10.1038/natrevmats.2016.76.

[7] W. Jiang, H. Yuan, C.K. Chan, C.A. von Roemeling, Z. Yan, I.L. Weissman, B.Y.S. Kim, Lessons from immuno-oncology: a new era for cancer nanomedicine?, Nat. Rev. Drug Discov. 16 (2017) 369–370. doi:10.1038/nrd.2017.34.

[8] K. Shao, S. Singha, X. Clemente-Casares, S. Tsai, Y. Yang, P. Santamaria, Nanoparticle-Based Immunotherapy for Cancer, ACS Nano. 9 (2015) 16–30. doi:10.1021/nn5062029.

[9] C. Maisonneuve, S. Bertholet, D.J. Philpott, E. De Gregorio, Unleashing the potential of NOD- and Toll-like agonists as vaccine adjuvants., Proc. Natl. Acad. Sci. U. S. A. 111 (2014) 12294–9. doi:10.1073/pnas.1400478111.

[10] Q. Hu, M. Wu, C. Fang, C. Cheng, M. Zhao, W. Fang, P.K. Chu, Y. Ping, G. Tang, Engineering Nanoparticle-Coated Bacteria as Oral DNA Vaccines for Cancer Immunotherapy, Nano Lett. 15 (2015) 2732–2739. doi:10.1021/acs.nanolett.5b00570.

[11] N.-H. Cho, T.-C. Cheong, J.H. Min, J.H. Wu, S.J. Lee, D. Kim, J.-S. Yang, S. Kim, Y.K. Kim, S.-Y. Seong, A multifunctional core–shell nanoparticle for dendritic cell-based cancer immunotherapy, Nat. Nanotechnol. 6 (2011) 675–682. doi:10.1038/nnano.2011.149.

[12] A. de Titta, M. Ballester, Z. Julier, C. Nembrini, L. Jeanbart, A.J. van der Vlies, M.A. Swartz, J.A. Hubbell, Nanoparticle conjugation of CpG enhances adjuvancy for cellular immunity and memory recall at low dose., Proc. Natl. Acad. Sci. U. S. A. 110 (2013) 19902–7. doi:10.1073/pnas.1313152110.

[13] J.A. Hubbell, S.N. Thomas, M.A. Swartz, Materials engineering for immunomodulation, Nature. 462 (2009) 449–460. doi:10.1038/nature08604.

[14] R.H. Fang, A. V Kroll, L. Zhang, Nano-immunoengineering: Nanoparticle-Based Manipulation of Antigen-Presenting Cells for Cancer Immunotherapy (Small 41/2015)., Small. 11 (2015) 5466. doi:10.1002/smll.201570249.

[15] J. Leleux, K. Roy, Micro and Nanoparticle-Based Delivery Systems for Vaccine Immunotherapy: An Immunological and Materials Perspective, Adv. Healthc. Mater. 2 (2013) 72–94. doi:10.1002/adhm.201200268.

[16] D.J. Irvine, M.C. Hanson, K. Rakhra, T. Tokatlian, Synthetic Nanoparticles for Vaccines and Immunotherapy., Chem. Rev. 115 (2015) 11109–46. doi:10.1021/acs.chemrev.5b00109.

[17] W. Song, S.N. Musetti, L. Huang, Nanomaterials for cancer immunotherapy, Biomaterials. 148 (2017) 16–30. doi:10.1016/J.BIOMATERIALS.2017.09.017.

[18] M.S. Goldberg, Immunoengineering: How nanotechnology can enhance cancer

[19] J.F. Hainfeld, M.J. O'Connor, F.A. Dilmanian, D.N. Slatkin, D.J. Adams, H.M. Smilowitz, Micro-CT enables microlocalisation and quantification of Her2-targeted gold nanoparticles within tumour regions., Br. J. Radiol. 84 (2011) 526–33. doi:10.1259/bjr/42612922.

[20] A.C. Anselmo, S. Mitragotri, A Review of Clinical Translation of Inorganic Nanoparticles., AAPS J. 17 (2015) 1041–54. doi:10.1208/s12248-015-9780-2.

[21] M. Levy, N. Luciani, D. Alloyeau, D. Elgrabli, V. Deveaux, C. Pechoux, S. Chat, G. Wang, N. Vats, F. Gendron, C. Factor, S. Lotersztajn, A. Luciani, C. Wilhelm, F. Gazeau, Long term in vivo biotransformation of iron oxide nanoparticles, Biomaterials. 32 (2011) 3988–3999. doi:10.1016/j.biomaterials.2011.02.031.

[22] J.D. López-Castro, A. V. Maraloiu, J.J. Delgado, J.J. Calvino, M.-G. Blanchin, N. Gálvez, J.M. Domínguez-Vera, From synthetic to natural nanoparticles: monitoring the biodegradation of SPIO (P904) into ferritin by electron microscopy, Nanoscale. 3 (2011) 4597. doi:10.1039/c1nr10980d.

[23] P. Bourrinet, H.H. Bengele, B. Bonnemain, A. Dencausse, J.-M. Idee, P.M. Jacobs, J.M. Lewis, Preclinical safety and pharmacokinetic profile of ferumoxtran-10, an ultrasmall superparamagnetic iron oxide magnetic resonance contrast agent., Invest. Radiol. 41 (2006) 313–324. doi:10.1097/01.rli.0000197669.80475.dd.

[24] J.-H. Lee, Y.-M. Huh, Y. Jun, J. Seo, J. Jang, H.-T. Song, S. Kim, E.-J. Cho, H.-G. Yoon, J.-S. Suh, J. Cheon, Artificially engineered magnetic nanoparticles for ultra-sensitive molecular imaging., Nat. Med. 13 (2007) 95–99. doi:10.1038/nm1467.

[25] J. Huang, X. Zhong, L. Wang, L. Yang, H. Mao, Improving the magnetic resonance imaging contrast and detection methods with engineered magnetic nanoparticles, Theranostics. 2 (2012) 86–102. doi:10.7150/thno.4006.

[26] S. Zanganeh, G. Hutter, R. Spitler, O. Lenkov, M. Mahmoudi, A. Shaw, J.S. Pajarinen, H. Nejadnik, S. Goodman, M. Moseley, L.M. Coussens, H.E. Daldrup-Link, Iron oxide nanoparticles inhibit tumour growth by inducing pro-inflammatory macrophage polarization in tumour tissues., Nat. Nanotechnol. 11 (2016) 986–994. doi:10.1038/nnano.2016.168.

[27] J. Huang, Y. Li, A. Orza, Q. Lu, P. Guo, L. Wang, L. Yang, H. Mao, Magnetic Nanoparticle Facilitated Drug Delivery for Cancer Therapy with Targeted and Image-Guided Approaches, Adv. Funct. Mater. 26 (2016) 3818–3836. doi:10.1002/adfm.201504185.

[28] Y. Qian, H. Jin, S. Qiao, Y. Dai, C. Huang, L. Lu, Q. Luo, Z. Zhang, Targeting dendritic cells in lymph node with an antigen peptide-based nanovaccine for cancer immunotherapy, Biomaterials. 98 (2016) 171–183. doi:10.1016/J.BIOMATERIALS.2016.05.008.

[29] J.F.B. Banchereau, Immunobiology of Dendritic Cells, Annu. Rev. Immunol. 18 (2000) 767–811. doi:10.1146/annurev.immunol.18.1.767.

[30] H. Kanzler, F.J. Barrat, E.M. Hessel, R.L. Coffman, Therapeutic targeting of innate immunity with Toll-like receptor agonists and antagonists., Nat. Med. 13 (2007) 552–9.

[31] S.P. Kasturi, I. Skountzou, R.A. Albrecht, D. Koutsonanos, T. Hua, H.I. Nakaya, R. Ravindran, S. Stewart, M. Alam, M. Kwissa, F. Villinger, N. Murthy, J. Steel, J. Jacob, R.J. Hogan, A. García-Sastre, R. Compans, B. Pulendran, Programming the magnitude and persistence of antibody responses with innate immunity., Nature. 470 (2011) 543–7. doi:10.1038/nature09737.

[32] R. Medzhitov, Toll-like receptors and innate immunity., Nat. Rev. Immunol. 1 (2001) 135–145. doi:10.1038/35100529.

[33] L. a J. O'Neill, D. Golenbock, A.G. Bowie, The history of Toll-like receptors - redefining innate immunity., Nat. Rev. Immunol. 13 (2013) 453–60. doi:10.1038/nri3446.

[34] F. Steinhagen, T. Kinjo, C. Bode, D.M. Klinman, TLR-based immune adjuvants., Vaccine. 29 (2011) 3341–55. doi:10.1016/j.vaccine.2010.08.002.

[35] Q. Zeng, H. Li, H. Jiang, J. Yu, Y. Wang, H. Ke, T. Gong, Z. Zhang, X. Sun, Tailoring polymeric hybrid micelles with lymph node targeting ability to improve the potency of cancer vaccines, Biomaterials. 122 (2017) 105–113. doi:10.1016/J.BIOMATERIALS.2017.01.010.

[36] S.W. Brubaker, K.S. Bonham, I. Zanoni, J.C. Kagan, Innate immune pattern recognition: a cell biological perspective., Annu. Rev. Immunol. 33 (2015) 257–90. doi:10.1146/annurev-immunol-032414-112240.

[37] Q. Zhu, C. Egelston, A. Vivekanandhan, S. Uematsu, S. Akira, D.M. Klinman, I.M. Belyakov, J. a Berzofsky, Toll-like receptor ligands synergize through distinct dendritic cell pathways to induce T cell responses: implications for vaccines., Proc. Natl. Acad. Sci. U. S. A. 105 (2008) 16260–16265. doi:10.1073/pnas.0805325105.

[38] G. Napolitani, A. Rinaldi, F. Bertoni, F. Sallusto, A. Lanzavecchia, Selected Toll-like receptor agonist combinations synergistically trigger a T helper type 1-polarizing program in dendritic cells., Nat. Immunol. 6 (2005) 769–76. doi:10.1038/ni1223.

[39] T. Warger, P. Osterloh, G. Rechtsteiner, M. Fassbender, V. Heib, B. Schmid, E. Schmitt, H. Schild, M.P. Radsak, Synergistic activation of dendritic cells by combined Toll-like receptor ligation induces superior CTL responses in vivo, Blood. 108 (2006) 544–550. doi:10.1182/blood-2005-10-4015.

[40] G.M. Lynn, R. Laga, P.A. Darrah, A.S. Ishizuka, A.J. Balaci, A.E. Dulcey, M. Pechar, R. Pola, M.Y. Gerner, A. Yamamoto, C.R. Buechler, K.M. Quinn, M.G. Smelkinson, O. Vanek, R. Cawood, T. Hills, O. Vasalatiy, K. Kastenmüller, J.R. Francica, L. Stutts, J.K. Tom, K.A. Ryu, A.P. Esser-Kahn, T. Etrych, K.D. Fisher, L.W. Seymour, R.A. Seder, In vivo characterization of the physicochemical properties of polymer-linked TLR agonists that enhance vaccine immunogenicity, Nat. Biotechnol. 33 (2015) 1201–1210. doi:10.1038/nbt.3371.

[41] Y. Hu, X. Cong, L. Chen, J. Qi, X. Wu, M. Zhou, D. Yoo, F. Li, W. Sun, J. Wu, X. Zhao, Z. Chen, J. Yu, Y. Du, J. Wang, Synergy of TLR3 and 7 ligands significantly enhances function of DCs to present inactivated PRRSV antigen through TRIF/MyD88-NF-κB signaling pathway., Sci. Rep. 6 (2016) 23977. doi:10.1038/srep23977.

[42] M.A. Cheever, Twelve immunotherapy drugs that could cure cancers., Immunol. Rev. 222

[43] F.J. Tacken, I.S. Zeelenberg, E.J. Cruz, M.A. van Hout-Kuijer, G. van de Glind, R.G. Fokkink, A.J.A. Lambeck, C.G. Figdor, Targeted delivery of TLR ligands to human and mouse dendritic cells strongly enhances adjuvanticity., Blood. 118 (2011) 6836–44. doi:10.1182/blood-2011-07-367615.

[44] C.-C. Chang, M. Campoli, S. Ferrone, HLA class I antigen expression in malignant cells: why does it not always correlate with CTL-mediated lysis?, Curr. Opin. Immunol. 16 (2004) 644–650. doi:10.1016/j.coi.2004.07.015.

[45] Y. Iwai, M. Ishida, Y. Tanaka, T. Okazaki, T. Honjo, N. Minato, Involvement of PD-L1 on tumor cells in the escape from host immune system and tumor immunotherapy by PD-L1 blockade., Proc. Natl. Acad. Sci. U. S. A. 99 (2002) 12293–7. doi:10.1073/pnas.192461099.

[46] W. Zou, L. Chen, Inhibitory B7-family molecules in the tumour microenvironment, Nat. Rev. Immunol. 8 (2008) 467–477. doi:10.1038/nri2326.

[47] C. Nembrini, A. Stano, K.Y. Dane, M. Ballester, A.J. van der Vlies, B.J. Marsland, M.A. Swartz, J.A. Hubbell, Nanoparticle conjugation of antigen enhances cytotoxic T-cell responses in pulmonary vaccination., Proc. Natl. Acad. Sci. U. S. A. 108 (2011) E989-97. doi:10.1073/pnas.1104264108.

[48] P. Johansen, T. Storni, L. Rettig, Z. Qiu, A. Der-Sarkissian, K.A. Smith, V. Manolova, K.S. Lang, G. Senti, B. Müllhaupt, T. Gerlach, R.F. Speck, A. Bot, T.M. Kündig, Antigen kinetics determines immune reactivity., Proc. Natl. Acad. Sci. U. S. A. 105 (2008) 5189–94. doi:10.1073/pnas.0706296105.

[49] Y. Yang, C.-T. Huang, X. Huang, D.M. Pardoll, Persistent Toll-like receptor signals are required for reversal of regulatory T cell–mediated CD8 tolerance, Nat. Immunol. 5 (2004) 508–515. doi:10.1038/ni1059.

[50] Mechanisms and Consequences of Dendritic Cell Migration, Immunity. 29 (2008) 325–342. doi:10.1016/J.IMMUNI.2008.08.006.

[51] C.M. Jewell, S.C.B. López, D.J. Irvine, In situ engineering of the lymph node microenvironment via intranodal injection of adjuvant-releasing polymer particles., Proc. Natl. Acad. Sci. U. S. A. 108 (2011) 15745–50. doi:10.1073/pnas.1105200108.

[52] Renal clearable inorganic nanoparticles: a new frontier of bionanotechnology, Mater. Today. 16 (2013) 477–486. doi:10.1016/J.MATTOD.2013.11.003.

[53] H.S. Choi, W. Liu, P. Misra, E. Tanaka, J.P. Zimmer, B. Itty Ipe, M.G. Bawendi, J. V Frangioni, Renal clearance of quantum dots., Nat. Biotechnol. 25 (2007) 1165–70. doi:10.1038/nbt1340.

[54] A.P. Grosvenor, B.A. Kobe, M.C. Biesinger, N.S. McIntyre, Investigation of multiplet splitting of Fe 2p XPS spectra and bonding in iron compounds, Surf. Interface Anal. 36 (2004) 1564–1574. doi:10.1002/sia.1984.

[55] M. Descostes, F. Mercier, N. Thromat, C. Beaucaire, M. Gautier-Soyer, Use of XPS in the determination of chemical environment and oxidation state of iron and sulfur samples: constitution of a data basis in binding energies for Fe and S reference compounds and applications to the evidence of surface species of an oxidized py, Appl. Surf. Sci. 165

[56] J.M. Byrne, V.S. Coker, E. Cespedes, P.L. Wincott, D.J. Vaughan, R.A.D. Pattrick, G. van der Laan, E. Arenholz, F. Tuna, M. Bencsik, J.R. Lloyd, N.D. Telling, Biosynthesis of Zinc Substituted Magnetite Nanoparticles with Enhanced Magnetic Properties, Adv. Funct. Mater. 24 (2014) 2518–2529. doi:10.1002/adfm.201303230.

[57] H. Lv, L. Ma, P. Zeng, D. Ke, T. Peng, Synthesis of floriated ZnFe2O4 with porous nanorod structures and its photocatalytic hydrogen production under visible light, J. Mater. Chem. 20 (2010) 3665. doi:10.1039/b919897k.

[58] M. Cobaleda-Siles, M. Henriksen-Lacey, A.R. de Angulo, A. Bernecker, V.G. Vallejo, B. Szczupak, J. Llop, G. Pastor, S. Plaza-Garcia, M. Jauregui-Osoro, L.K. Meszaros, J.C. Mareque-Rivas, An Iron Oxide Nanocarrier for dsRNA to Target Lymph Nodes and Strongly Activate Cells of the Immune System., Small. 10 (2014) 5054–67. doi:10.1002/smll.201401353.

[59] A. Kuznik, M. Bencina, U. Svajger, M. Jeras, B. Rozman, R. Jerala, Mechanism of endosomal TLR inhibition by antimalarial drugs and imidazoquinolines., J. Immunol. 186 (2011) 4794–804. doi:10.4049/jimmunol.1000702.

[60] N.J. Gay, M.F. Symmons, M. Gangloff, C.E. Bryant, Assembly and localization of Toll-like receptor signalling complexes., Nat. Rev. Immunol. 14 (2014) 546–58. doi:10.1038/nri3713.

[61] T. Nishiya, E. Kajita, S. Miwa, A.L. Defranco, TLR3 and TLR7 are targeted to the same intracellular compartments by distinct regulatory elements., J. Biol. Chem. 280 (2005) 37107–17. doi:10.1074/jbc.M504951200.

[62] M.P. Schön, M. Schön, TLR7 and TLR8 as targets in cancer therapy., Oncogene. 27 (2008) 190–9. doi:10.1038/sj.onc.1210913.

[63] R. Ammi, J. De Waele, Y. Willemen, I. Van Brussel, D.M. Schrijvers, E. Lion, E.L.J. Smits, Poly(I:C) as cancer vaccine adjuvant: knocking on the door of medical breakthroughs., Pharmacol. Ther. 146 (2015) 120–31. doi:10.1016/j.pharmthera.2014.09.010.

[64] G. Driessens, J. Kline, T.F. Gajewski, Costimulatory and coinhibitory receptors in anti-tumor immunity., Immunol. Rev. 229 (2009) 126–44. doi:10.1111/j.1600-065X.2009.00771.x.

[65] P.D. Cravens, P.E. Lipsky, Dendritic cells, chemokine receptors and autoimmune inflammatory diseases, Immunol. Cell Biol. 80 (2002) 497–505. doi:10.1046/j.1440-1711.2002.01118.x.

[66] H. Kitamura, H. Morikawa, H. Kamon, M. Iguchi, S. Hojyo, T. Fukada, S. Yamashita, T. Kaisho, S. Akira, M. Murakami, T. Hirano, Toll-like receptor–mediated regulation of zinc homeostasis influences dendritic cell function, Nat. Immunol. 7 (2006) 971–977. doi:10.1038/ni1373.

[67] B. Salaun, I. Coste, M.-C. Rissoan, S.J. Lebecque, T. Renno, TLR3 can directly trigger apoptosis in human cancer cells., J. Immunol. 176 (2006) 4894–901. http://www.ncbi.nlm.nih.gov/pubmed/16585585 (accessed February 12, 2014).

[68] C. Trumpfheller, M. Caskey, G. Nchinda, M.P. Longhi, O. Mizenina, Y. Huang, S.J.

Proc. Natl. Acad. Sci. U. S. A. 105 (2008) 2574–9. doi:10.1073/pnas.0711976105.

[69] S. Palchetti, D. Starace, P. De Cesaris, A. Filippini, E. Ziparo, A. Riccioli, Transfected poly(I:C) activates different dsRNA receptors, leading to apoptosis or immunoadjuvant response in androgen-independent prostate cancer cells., J. Biol. Chem. 290 (2015) 5470–83. doi:10.1074/jbc.M114.601625.

[70] A. Ruiz-de-Angulo, A. Zabaleta, V. Gómez-Vallejo, J. Llop, J.C. Mareque-Rivas, Microdosed Lipid-Coated ^{67} Ga-Magnetite Enhances Antigen-Specific Immunity by Image Tracked Delivery of Antigen and CpG to Lymph Nodes, ACS Nano. 10 (2016) 1602–1618. doi:10.1021/acsnano.5b07253.

[71] F. Nimmerjahn, Divergent Immunoglobulin G Subclass Activity Through Selective Fc Receptor Binding, Science (80-.). 310 (2005) 1510–1512. doi:10.1126/science.1118948.

[72] F. Aranda, D. Llopiz, N. Díaz-Valdés, J.I. Riezu-Boj, J. Bezunartea, M. Ruiz, M. Martínez, M. Durantez, C. Mansilla, J. Prieto, J.J. Lasarte, F. Borrás-Cuesta, P. Sarobe, Adjuvant combination and antigen targeting as a strategy to induce polyfunctional and high-avidity T-cell responses against poorly immunogenic tumors., Cancer Res. 71 (2011) 3214–24. doi:10.1158/0008-5472.CAN-10-3259.

[73] F. Sallusto, J. Geginat, A. Lanzavecchia, C entral M emory and E ffector M emory T C ell S ubsets : Function, Generation, and Maintenance, Annu. Rev. Immunol. 22 (2004) 745–763. doi:10.1146/annurev.immunol.22.012703.104702.

[74] M.A. Postow, M.K. Callahan, J.D. Wolchok, Immune Checkpoint Blockade in Cancer Therapy, J. Clin. Oncol. 33 (2015) 1974–1982. doi:10.1200/JCO.2014.59.4358.

[75] D.M. Pardoll, The blockade of immune checkpoints in cancer immunotherapy, Nat. Rev. Cancer. 12 (2012) 252–264. doi:10.1038/nrc3239.

[76] T. Yamazaki, H. Akiba, H. Iwai, H. Matsuda, M. Aoki, Y. Tanno, T. Shin, H. Tsuchiya, D.M. Pardoll, K. Okumura, M. Azuma, H. Yagita, Expression of programmed death 1 ligands by murine T cells and APC., J. Immunol. 169 (2002) 5538–45. doi:10.4049/JIMMUNOL.169.10.5538.

[77] G.J. Freeman, A.J. Long, Y. Iwai, K. Bourque, T. Chernova, H. Nishimura, L.J. Fitz, N. Malenkovich, T. Okazaki, M.C. Byrne, H.F. Horton, L. Fouser, L. Carter, V. Ling, M.R. Bowman, B.M. Carreno, M. Collins, C.R. Wood, T. Honjo, Engagement of the PD-1 immunoinhibitory receptor by a novel B7 family member leads to negative regulation of lymphocyte activation., J. Exp. Med. 192 (2000) 1027–34. doi:10.1084/jem.192.7.1027.

[78] M. Gato-Cañas, M. Zuazo, H. Arasanz, M. Ibañez-Vea, L. Lorenzo, G. Fernandez-Hinojal, R. Vera, C. Smerdou, E. Martisova, I. Arozarena, C. Wellbrock, D. Llopiz, M. Ruiz, P. Sarobe, K. Breckpot, G. Kochan, D. Escors, PDL1 Signals through Conserved Sequence Motifs to Overcome Interferon-Mediated Cytotoxicity, Cell Rep. 20 (2017) 1818–1829. doi:10.1016/J.CELREP.2017.07.075.

[79] F.A. Ran, P.D. Hsu, J. Wright, V. Agarwala, D.A. Scott, F. Zhang, Genome engineering using the CRISPR-Cas9 system, Nat. Protoc. 8 (2013) 2281–2308. doi:10.1038/nprot.2013.143.

editing, Gene Ther. 23 (2016) 627–633. doi:10.1038/gt.2016.27.

[81] S.M. Makela, M. Strengell, T.E. Pietila, P. Osterlund, I. Julkunen, Multiple signaling pathways contribute to synergistic TLR ligand-dependent cytokine gene expression in human monocyte-derived macrophages and dendritic cells, J. Leukoc. Biol. 85 (2009) 664–672. doi:10.1189/jlb.0808503.

[82] S.N. Thomas, E. Vokali, A.W. Lund, J.A. Hubbell, M.A. Swartz, Targeting the tumor-draining lymph node with adjuvanted nanoparticles reshapes the anti-tumor immune response, Biomaterials. 35 (2014) 814–824. doi:10.1016/j.biomaterials.2013.10.003.

[83] Y. Fan, J.J. Moon, Nanoparticle Drug Delivery Systems Designed to Improve Cancer Vaccines and Immunotherapy., Vaccines. 3 (2015) 662–85. doi:10.3390/vaccines3030662.

[84] S. Akira, K. Takeda, Toll-like receptor signalling, Nat. Rev. Immunol. 4 (2004) 499–511. doi:10.1038/nri1391.

[85] S. McCartney, W. Vermi, S. Gilfillan, M. Cella, T.L. Murphy, R.D. Schreiber, K.M. Murphy, M. Colonna, Distinct and complementary functions of MDA5 and TLR3 in poly(I:C)-mediated activation of mouse NK cells., J. Exp. Med. 206 (2009) 2967–76. doi:10.1084/jem.20091181.

[86] C.L. Ahonen, S.J. Gibson, R.M. Smith, L.K. Pederson, J.M. Lindh, M.A. Tomai, J.P. Vasilakos, Dendritic Cell Maturation and Subsequent Enhanced T-Cell Stimulation Induced with the Novel Synthetic Immune Response Modifier R-848, Cell. Immunol. 197 (1999) 62–72.

[87] S.J. Gibson, J.M. Lindh, T.R. Riter, R.M. Gleason, L.M. Rogers, A.E. Fuller, J.L. Oesterich, K.B. Gorden, X. Qiu, S.W. Mckane, R.J. Noelle, R.L. Miller, R.M. Kedl, P. Fitzgerald-Bocarsly, M.A. Tomai, J.P. Vasilakos, Plasmacytoid dendritic cells produce cytokines and mature in response to the TLR7 agonists, imiquimod and resiquimod, Cell. Immunol. 218 (2002) 74–86.

[88] M. Wysocka, S. Newton, B.M. Benoit, C. Introcaso, A.S. Hancock, J. Chehimi, S.K. Richardson, J.M. Gelfand, L.J. Montaner, A.H. Rook, Synthetic Imidazoquinolines Potently and Broadly Activate the Cellular Immune Response of Patients with Cutaneous T-Cell Lymphoma: Synergy with Interferon-y Enhances Production of Interleukin-12, Clin. Lymphoma Myeloma. 7 (2007) 524–534.

[89] T.L. Wagner, V.L. Horton, G.L. Carlson, P.E. Myhre, S.J. Gibson, L.M. Imbertson, M.A. Tomai, Induction of cytokines in cynomolgus monkeys by the immune response modifiers, imiquimod, S-27609 and S-28463, Cytokine. 9 (1997) 837–845.

[90] G. Stary, C. Bangert, M. Tauber, R. Strohal, T. Kopp, G. Stingl, Tumoricidal activity of TLR7/8-activated inflammatory dendritic cells., J. Exp. Med. 204 (2007) 1441–1451.

[91] U.R. Hengge, T. Ruzicka, Topical immunomodulation in dermatology: Potential of Toll-like receptor agonists, Dermatologic Surg. 30 (2004) 1101–1112.

[92] G.A. Bishop, L.M. Ramirez, M. Baccam, L.K. Busch, L.K. Pederson, M.A. Tomai, The Immune Response Modifier Resiquimod Mimics CD40-Induced B Cell Activation, Cell.

Cells From TLR Tolerance, J. Immunol. 183 (2009) 2974–2983.

[94] J.A. Hanten, J.P. Vasilakos, C.L. Riter, L. Neys, K.E. Lipson, S.S. Alkan, W. Birmachu, Comparison of human B cell activation by TLR7 and TLR9 agonists, BMC Immunol. 9 (2008) 1–15.

[95] J.-H. Han, J. Lee, S.-J. Jeon, E.-S. Choi, S.-D. Cho, B.-Y. Kim, D.-J. Kim, J.-H. Park, J.-H. Park, In vitro and in vivo growth inhibition of prostate cancer by the small molecule imiquimod, Int. J. Oncol. 42 (2013) 2087–2093.

[96] T. Meyer, I. Nindl, T. Schmook, C. Ulrich, W. Sterry, E. Stockfleth, Induction of apoptosis by Toll-like receptor-7 agonist in tissue cultures., Br. J. Dermatol. 149 (2003) 9–13.

[97] M. Schon, A.B. Bong, C. Drewniok, J. Herz, C.C. Geilen, J. Reifenberger, B. Benninghoff, H.B. Slade, H. Gollnick, M.P. Schon, Tumor-Selective Induction of Apoptosis and the Small-Molecule Immune Response Modifier Imiquimod, J. Natl. Cancer Inst. 95 (2003) 1138–1149.

[98] C. Hesling, M. D'Incan, S. Mansard, F. Franck, A. Corbin-Duval, C. Chevenet, P. Dechelotte, J.-C. Madelmont, A. Veyre, P. Souteyrand, Y.-J. Bignon, In vivo and in situ modulation of the expression of genes involved in metastasis and angiogenesis in a patient treated with topical imiquimod for melanoma skin metastases, Br. J. Dermatol. 150 (2004) 761–767. doi:10.1111/j.0007-0963.2004.05898.x.

[99] I.H. Wolf, J. Smolle, B. Binder, L. Cerroni, E. Richtig, H. Kerl, Topical Imiquimod in the Treatment of Metastatic Melanoma to Skin, Arch. Dermatol. 139 (2003) 273. doi:10.1001/archderm.139.3.273.

[100] C. Bourquin, C. Hotz, D. Noerenberg, A. Voelkl, S. Heidegger, L.C. Roetzer, B. Storch, N. Sandholzer, C. Wurzenberger, D. Anz, S. Endres, Systemic cancer therapy with a small molecule agonist of toll-like receptor 7 can be improved by circumventing TLR tolerance., Cancer Res. 71 (2011) 5123–33. doi:10.1158/0008-5472.CAN-10-3903.

[101] M. Kim, H.-B. Moon, K. Kim, K.-Y. Lee, Antigen dose governs the shaping of CTL repertoires in vitro and in vivo, Int. Immunol. 18 (2006) 435–444. doi:10.1093/intimm/dxh383.

[102] R. Billeskov, Y. Wang, S. Solaymani-Mohammadi, B. Frey, S. Kulkarni, P. Andersen, E.M. Agger, Y. Sui, J.A. Berzofsky, Low Antigen Dose in Adjuvant-Based Vaccination Selectively Induces CD4 T Cells with Enhanced Functional Avidity and Protective Efficacy., J. Immunol. 198 (2017) 3494–3506. doi:10.4049/jimmunol.1600965.

[103] J.P.M. Almeida, A.Y. Lin, E.R. Figueroa, A.E. Foster, R.A. Drezek, In vivo Gold Nanoparticle Delivery of Peptide Vaccine Induces Anti-Tumor Immune Response in Prophylactic and Therapeutic Tumor Models, Small. 11 (2015) 1453–1459. doi:10.1002/smll.201402179.

[104] S. Yan, B.E. Rolfe, B. Zhang, Y.H. Mohammed, W. Gu, Z.P. Xu, Polarized immune responses modulated by layered double hydroxides nanoparticle conjugated with CpG, Biomaterials. 35 (2014) 9508–9516. doi:10.1016/j.biomaterials.2014.07.055.

properties of nano-vaccines against tumors., J. Immunol. 173 (2004) 3148–54. http://www.ncbi.nlm.nih.gov/pubmed/15322175 (accessed November 16, 2017).

[106] R.A. Rosalia, L.J. Cruz, S. van Duikeren, A.T. Tromp, A.L. Silva, W. Jiskoot, T. de Gruijl, C. Löwik, J. Oostendorp, S.H. van der Burg, F. Ossendorp, CD40-targeted dendritic cell delivery of PLGA-nanoparticle vaccines induce potent anti-tumor responses, Biomaterials. 40 (2015) 88–97. doi:10.1016/j.biomaterials.2014.10.053.

[107] J.M. Silva, E. Zupancic, G. Vandermeulen, V.G. Oliveira, A. Salgado, M. Videira, M. Gaspar, L. Graca, V. Préat, H.F. Florindo, In vivo delivery of peptides and Toll-like receptor ligands by mannose-functionalized polymeric nanoparticles induces prophylactic and therapeutic anti-tumor immune responses in a melanoma model, J. Control. Release. 198 (2015) 91–103. doi:10.1016/j.jconrel.2014.11.033.

[108] S. Rahimian, M.F. Fransen, J.W. Kleinovink, J.R. Christensen, M. Amidi, W.E. Hennink, F. Ossendorp, Polymeric nanoparticles for co-delivery of synthetic long peptide antigen and poly IC as therapeutic cancer vaccine formulation, J. Control. Release. 203 (2015) 16–22. doi:10.1016/j.jconrel.2015.02.006.

[109] P. Zhang, Y.-C. Chiu, L.H. Tostanoski, C.M. Jewell, Polyelectrolyte Multilayers Assembled Entirely from Immune Signals on Gold Nanoparticle Templates Promote Antigen-Specific T Cell Response, ACS Nano. 9 (2015) 6465–6477. doi:10.1021/acsnano.5b02153.

[110] D. Alvarez, E.H. Vollmann, U.H. von Andrian, Mechanisms and consequences of dendritic cell migration., Immunity. 29 (2008) 325–42. doi:10.1016/j.immuni.2008.08.006.

[111] B.D. Shields, F. Mahmoud, E.M. Taylor, S.D. Byrum, D. Sengupta, B. Koss, G. Baldini, S. Ransom, K. Cline, S.G. Mackintosh, R.D. Edmondson, S. Shalin, A.J. Tackett, Indicators of responsiveness to immune checkpoint inhibitors, Sci. Rep. 7 (2017) 807. doi:10.1038/s41598-017-01000-2.

[112] J.S. Temel, J.F. Gainor, R.J. Sullivan, J.A. Greer, Keeping Expectations in Check With Immune Checkpoint Inhibitors, J. Clin. Oncol. (2018) JCO.2017.76.214. doi:10.1200/JCO.2017.76.2146.

[113] T. Nagato, Y.-R. Lee, Y. Harabuchi, E. Celis, Combinatorial immunotherapy of polyinosinic-polycytidylic acid and blockade of programmed death-ligand 1 induce effective CD8 T-cell responses against established tumors., Clin. Cancer Res. 20 (2014) 1223–34. doi:10.1158/1078-0432.CCR-13-2781.

[114] A.R. Sánchez-Paulete, F.J. Cueto, M. Martínez-López, S. Labiano, A. Morales-Kastresana, M.E. Rodríguez-Ruiz, M. Jure-Kunkel, A. Azpilikueta, M.A. Aznar, J.I. Quetglas, D. Sancho, I. Melero, Cancer Immunotherapy with Immunomodulatory Anti-CD137 and Anti-PD-1 Monoclonal Antibodies Requires BATF3-Dependent Dendritic Cells., Cancer Discov. 6 (2016) 71–9. doi:10.1158/2159-8290.CD-15-0510.

[115] J. Lau, J. Cheung, A. Navarro, S. Lianoglou, B. Haley, K. Totpal, L. Sanders, H. Koeppen, P. Caplazi, J. McBride, H. Chiu, R. Hong, J. Grogan, V. Javinal, R. Yauch, B. Irving, M. Belvin, I. Mellman, J.M. Kim, M. Schmidt, Tumour and host cell PD-L1 is

[116] C. Bárcena, A.K. Sra, G.S. Chaubey, C. Khemtong, J.P. Liu, J. Gao, Zinc ferrite nanoparticles as MRI contrast agents, Chem. Commun. (Camb). (2008) 2224–2226. doi:10.1039/b801041b.

[117] S. Sun, H. Zeng, D.B. Robinson, S. Raoux, P.M. Rice, S.X. Wang, G. Li, Monodisperse MFe2O4 (M = Fe, Co, Mn) nanoparticles., J. Am. Chem. Soc. 126 (2004) 273–9. doi:10.1021/ja0380852.

[118] N. Gomez Blanco, M. Jauregui-Osoro, M. Cobaleda-Siles, C.R. Maldonado, M. Henriksen-Lacey, D. Padro, S. Clark, J.C. Mareque-Rivas, Iron oxide-filled micelles as ligands for fac-[M(CO)3]+ (M = (99m)Tc, Re)., Chem. Commun. (Camb). 48 (2012) 4211–3. doi:10.1039/c2cc31045g.